

## **Department of Precision and Microsystems Engineering**

### **Spatial flexure elements in a compliant motion stage**

T.A.A. Soek

Report no : 2020.017  
Coach : Ir. J. Rommers  
Professor : Prof. dr. ir. J.L. Herder  
Specialisation : Mechatronic System Design  
Type of report : Master Thesis  
Date : 26 Juni 2020





# Spatial flexure elements in a compliant motion stage

by

T.A.A. Soek

to obtain the degree of Master of Science  
at the Delft University of Technology,  
to be defended publicly on Friday June 26, 2020 at 3:00 PM.

Student number: 4541928  
Project duration: October, 2018 – June, 2020  
Supervisors: Prof. dr. ir. J.L. Herder,  
Ir. J. Rommers,

TU Delft  
TU Delft

An electronic version of this thesis is available at <http://repository.tudelft.nl/>.



# Preface

This thesis is the final result of my master Precision and Microsystem Engineering at the Technical University Delft, at the faculty of Mechanical, Maritime and Material Engineering. It is a true accomplishment for me personally and I am proud to graduate at one of the most technical disciplines here at TU Delft.

First and foremost, I would like to thank my daily supervisor Jelle for introducing me to this research area, his constructive criticism, our extensive weekly meetings, patience and careful guidance throughout my project. I would like to thank my chair, Just, for asking the difficult questions, his recommendations and general oversight. I would also like to thank the technical support staff, Bradley But, Gideon Emmaneel, Patrick van Holst, Rob Luttjeboer and Jos van Driel for their assistance with my experiments and 3D printing endeavours. I also want to give a special thanks to Eveline for her kind advice and guidance throughout my master programme. I would also like to thank my fellow students in room F34-F2 where I wrote the majority of my thesis. It was good to have a laugh every now and then but more importantly the brainstorming sessions were very valuable. I would also like to thank my friends for being there while I was in social isolation writing my thesis. Lastly, I want to thank my family for their support throughout the years and especially I would like to thank my parents for always believing in me. It has been quite a journey.

*T.A.A. Soek  
Delft, June 2020*



# Contents

<b>I Thesis</b>	<b>1</b>
<b>1 Introduction</b>	<b>3</b>
1.1 Research objectives . . . . .	3
1.2 Thesis outline . . . . .	3
<b>2 Paper</b>	<b>5</b>
A new approach: using helical flexure geometries in a 3DoF compliant motion stage . . . . .	5
<b>3 Discussion</b>	<b>23</b>
<b>4 Conclusion</b>	<b>25</b>
<b>II Appendix</b>	<b>27</b>





# Thesis





# Introduction

Planar (2D) flexure elements fulfil a pivotal role in the field of precision positioning systems as they do not suffer from backlash, friction or play and exhibit highly repeatable behaviour. However, planar building blocks are characterized by a limited design space as the majority of the flexure elements are flat and straight. In this thesis, it is proposed to investigate another type of flexure element that features spatial (3D) properties. This relatively new group of compliant shell mechanisms provide, in contrast to planar elementary flexures, much more geometric diversity. Furthermore, due to the recent improvements in fabrication possibilities (i.e. 3D steel printing) the usage of spatial compliant mechanisms are becoming a realistic and attractive alternative. Compliant shell mechanisms show promising indications that they may be used on an equal level with conventional flexure geometries. However, many shell surfaces remain to be studied and validated before they can be used to generate multi-degree of freedom flexure systems.

In this exploratory study a choice has been made to investigate helical flexure geometries. Looking into this particular group of surfaces is a logical step consistent with past research. Helical geometries show indications of potentially interesting properties. Additionally, these helical surfaces are elegantly expressed in terms of parametric equations that conveniently can be used to change the geometrical properties. Considering the lack of literature and the nature of complexity a decision was made to focus on linear small-displacement kinematic behaviour.

## 1.1. Research objectives

The main research objective of this paper focusses on the implementation of spatial flexures in motion stages. This main objective is split into two parts:

- Understanding of helical flexure geometries with varying curvature
- Use a helical flexure element to synthesize a compliant motion stage

## 1.2. Thesis outline

The main body of this thesis consists of one independent paper and serves as the key contribution of this master thesis. There are also recommendations for further research and a general outlook followed by conclusions. This paper is supplemented with an appendix providing insight into the work that was not included in the scientific paper.



# 2

## Paper

**A new approach: using helical flexure geometries in a 3DoF compliant motion stage**

# A new approach: using helical flexure geometries in a 3DoF compliant motion stage

Thomas Soek<sup>1</sup>, Jelle Rommers<sup>1</sup>, Just Herder<sup>1</sup>

<sup>1</sup>Department of Precision and Microsystems Engineering, Delft University of Technology

**Abstract** 2D flexure elements fulfil a pivotal role in the field of precision positioning systems as they do not suffer from backlash, friction or play and exhibit highly repeatable behaviour. However, planar building blocks are characterized by a limited design space as the majority of the flexure elements are flat and straight. In this paper, it is proposed to investigate another type of flexure element that features spatial (3D) properties. More specifically, it considers the use of helical flexure geometries in motion stages. Insight into the linear kinematic behaviour of various helical surfaces with varying curvature is provided with the usage of parametric optimization, screw theory, unified stiffness method and a performance metric. The newly acquired insights served as a prerequisite for selecting a suitable topology capable of guiding a stage. For demonstration purposes, a motion stage prototype was fabricated consisting of three helical flexure elements. Additionally, an eigenfrequency analysis was performed and experimentally validated with a model vibration test. This has led to the successful realization of a helical based compliant motion stage.

Topology (**FACT**) allows one to diagnose and synthesize multi-Degree of Freedom (**DoF**) flexure system concepts [4]. Literature hosts a variety of stage designs including, for instance, the double parallelogram and the cross pivot flexure [2, 3, 5]. Additionally, different modelling approaches have been employed. This has led, for example, to the design of the Infinity hinge by Brouwer et al [6] or a re-designed folded leaf spring using inverse finite element formulation by Rommers et al [7]. Although 2D flexure elements seem advantageous, they also have their limitations i.e. nonlinear kinematics (force-deflection) behaviour for a large **Range of Motion (RoM)** [8], non-constant support stiffness descending over a RoM [6] and parasitic error [5]. Additionally, 2D flexure elements are characterized by a limited design space. This space restriction is highlighted when defining a three-dimensional box geometry via a two dimensional rectangle with the third dimension normal to the sketch plane as a pre-defined constant. A constant out-of-plane third dimension is not desirable. To overcome these limitations it is necessary to look beyond the current use of planar flexure elements.

## 1 Introduction

In order to achieve precision, repeatability and predictability in precision engineering, compliant mechanisms play an important role. Their ability to transmit or guide spatial loads [1], while elastically deforming without the problems such as backlash, friction or play [2, 3]; justifies their popularity, particularly in precision positioning systems.

To date, the majority of stage designs are guided by planar (2D) mechanisms. These systems consist of one or a combination of serial and/or parallel elementary building blocks. Each element has clear constraints and freedom topologies. Examples include the wire flexure, leaf spring and folded leaf spring [2, 3]. Using methods such as the **Freedom And Constraint**

There is also another family of elementary flexures that exhibit spatial (3D) properties. This relatively new group of compliant shell mechanisms provide, in contrast to planar elementary flexures, much more geometric diversity. Furthermore, due to the recent improvements in fabrication possibilities (i.e. 3D steel printing) the usage of spatial compliant mechanisms are becoming a realistic and attractive alternative. Given that the vast majority of flexure elements are flat and straight it seems only logical to pursue this direction. The number of truly 3D elementary building blocks, however, remain scarce. In literature a few do occur, Hopkins et al [4] used spatial flexures to create a screw system. Rommers et al [8] introduced the so called 'Triflex' mechanism to create a linear guide. Nijssen et al [9] synthe-

sized a characterization method to explore the different types of compliant shell mechanisms. Additionally, the folded tape spring has been studied extensively [10, 11, 12, 13]. Herder and Radaelli also investigated the large-displacement behaviour of a spiral spring with variations of cross-section, orthotropy and pre-stress [14]. Compliant shell mechanisms exhibit encouraging indications that they may be used on an equal level with conventional flexure geometries. However, many shell surfaces remain to be studied and validated before they can be used to generate multi-DoF flexure systems.

In this exploratory study a choice has been made to investigate helical flexure geometries. Looking into this particular group of surfaces is a logical step consistent with past research [15]. Helical geometries show indications of potentially interesting properties. It would also be a sensible continuation of the work already done by Leemans [16] and Nijssen et al [9]. Additionally, these helical surfaces are elegantly expressed in terms of parametric equations that conveniently can be used to change the geometrical properties. Considering the lack of literature and the nature of complexity a decision was made to focus on linear small-displacement kinematic behaviour. The main research objective of this paper focusses on the implementation of spatial flexures in motion stages. This main objective is split into two parts. The first one looks into the understanding of helical flexure geometries with varying curvature. The second part highlights the more specific use of a helical flexure element and to generate, using such an element, a 3DoF compliant motion stage.

After the introduction this paper has four sections. The method in section 2 is split into three parts. The first part introduces the different families of helical surfaces along with the general equations and provides an explanation and overview of the chosen starting point. It also describes the basic helix, as well as the manual parametric optimization process towards the finalized version of the innovative **Spatially Curved Helix - (SCH)** flexure. In the second part a description is given on how by using eigen-screw decomposition and the already existing unified stiffness method it is possible to compare the principle directions of each helical surface. This unification method is a prerequisite for the compliance metric comparing the different geometries. Then the concept of the second moment of area will be used to explain how stiff-

ness properties change due to the introduction of curvature. The third and last part of the method section uses the knowledge gained in the form of an application by synthesising a 3DoF compliant motion stage. An eigenfrequency analysis was performed using Comsol, followed by an experiment to validate the numerical model. The results in section 3 summarize the findings of this study. Lastly, section 4 will be a discussion followed by the conclusions in section 5.

## 2 Method

### 2.1 Starting point

#### 2.1.1 Helix families

It is important to understand what exactly a helical surface is. Generally, there are 3 cases of uniform motion: (1) uniform translations, (2) uniform rotations with nonzero angular velocity about a fixed axis and (3) uniform helical motion that are the superposition of a uniform translation and uniform rotation parallel to the rotation's axis [17]. Commonly a line represents the path of a moving point, along similar analogy a surface represents the path of a moving line called a generatrix [17]. A generatrix can either be curved or a straight line. The generatrix curve or line **L** is revolved uniformly around an axis of revolution while translating along that direction of the axis. This axis is called a helical axis. Helical surfaces with a variable pitch have a non-constant relation of the translational speed to angular velocity. A choice was made not to consider helical surfaces with a variable pitch as it results in the addition of unwanted complexity. On the other hand, if the ratio of speed along the straight line to the value of the angular velocity is constant then this trajectory is known as an ordinary helical motion. This in turn produces an ordinary helical surface. Furthermore, every line projected on a helical surface can be taken as a generating line **L**. It is always possible to find a plane curve/lying in the plane of the axis of rotation [17]. If the generatrix is a straight line, it is called a ruled helical surface. If the generatrix is round or curved, it is known as a circular helical surface. Lastly, any surface formed by some curve profile, is called a helical surface with arbitrary plane generatrix curve. Figures 1, 2 and 3 show selected helical surfaces from each family and serve as an visual impression.

Figure 4 represents the different categories of helical surface geometries [17]. Within ordinary helical geometries, ruled helical surfaces contain

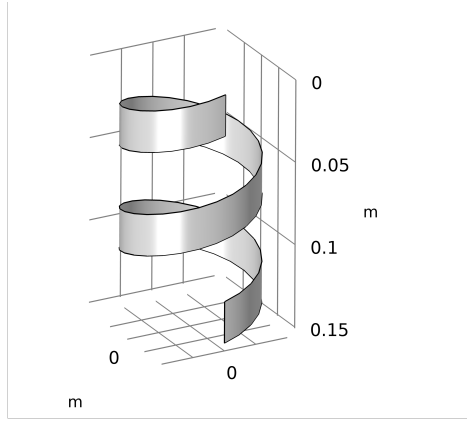


Figure 1: Ruled Helical surface  
The cylindrical helical strip

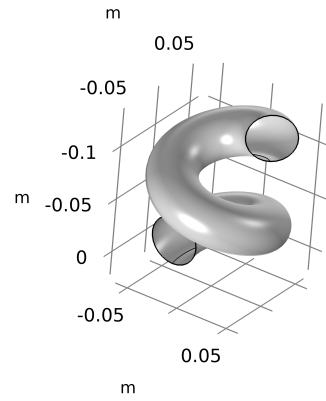


Figure 2: Circular Helical surface  
The tubular helical surface

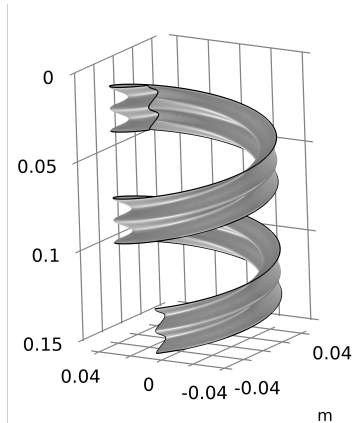


Figure 3: Helical surface with  
arbitrary plane generatrix curves  
The helical sinusoidal strip

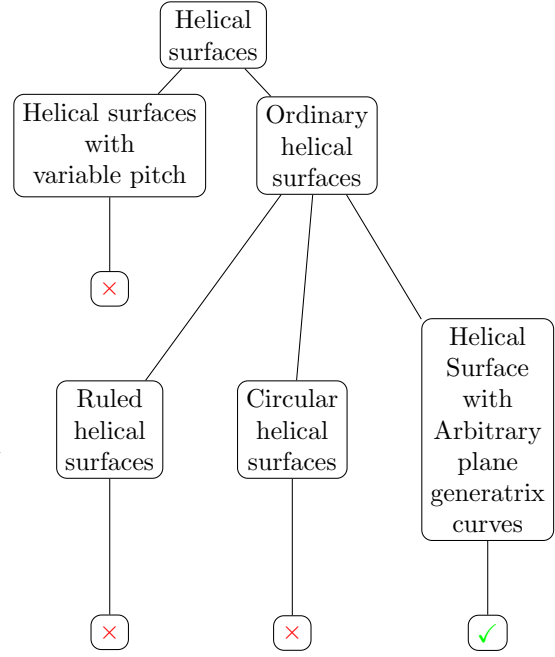


Figure 4: Helix families

too few parametric variables and therefore were not selected. Circular helical surfaces were not suitable as they are too rigid as well as mostly consisting of closed surfaces. Finally, this leaves the helical surfaces with an arbitrary plane generatrix plane as the most suitable option to pursue further.

### 2.1.2 General equations

Within the family of ordinary helical surfaces with arbitrary plane generatrix there are also many different curve profiles. Another choice is made to further investigate helical surfaces with a sinusoidal generatrix. Equation 1, 2 and 3 below fully describe the mathematical surface of this particular helix.

$$x = x(u, v) = \left( a + c \cos \frac{n\pi v}{d} \right) \cos(u) \quad (1)$$

$$y = y(u, v) = \left( a + c \cos \frac{n\pi v}{d} \right) \sin(u) \quad (2)$$

$$z = z(u, v) = b u + v \quad (3)$$

The following will expand on the meaning of these parameters.

- $a$  : affects the radius of the helix

- $c$  : determines amplitude of the sinusoid
- $n$  : number of semi-whole waves of a sinusoid located on a length  $d$ , where  $d$  is the corrugation curvature explained further below
- $b$  : influences width of the helix
- $u$  :  $[0, 2\pi k]$  - a linearly spaced vector, where  $k$  is the number of revolutions
- $v$  :  $[0, d]$  - a linearly spaced vector
- $d$  : corrugation curvature =  $2 b s b \pi$ , where  $sb$  is the pitch height multiplier

Parameters  $a$ ,  $c$ ,  $n$ ,  $b$ , and  $k$  are basic constants. Furthermore,  $u$  and  $v$  are vectors that together produce a two dimensional grid of coordinates. The last variable  $d$  benefits from some further explanation. The pitch multiplier  $sb$  allows one to change the pitch height. Hence, taking  $d = 2 b s b \pi$ , where  $sb = 1$ , it is possible to create a continuous helical surface with the strips just touching each other. If  $d > 2 b s b \pi$  the strips will overlap and vice versa when  $d < 2 b s b \pi$  the strips will move further away and underlap. By setting  $c = 0$  simplifies the parametric equations as they become representative for a cylindrical helical strip. More on this shall be discussed later in 2.1.3.

### 2.1.3 Backward iteration: complex helix towards basic helix

In this section the so-called most 'basic' helix will be introduced. By setting the amplitude of the sinusoid to  $c = 0$  equations 1, 2, 3 reduce to equations 4, 5, 6. The result shows a simplified version leaving only 3 equations that describe this surface, as can be seen in figure 5. These equations cannot be reduced further without losing the essential properties of a helical surface. This leads to the following definition:

$$x = x(u, v) = a \cos(u) \quad (4)$$

$$y = y(u, v) = a \sin(u) \quad (5)$$

$$z = z(u, v) = b u + v \quad (6)$$

**Definition:** the most basic helical surface is essentially a flat plate wrapped around a tin can, making it a short hollow cylinder with a small

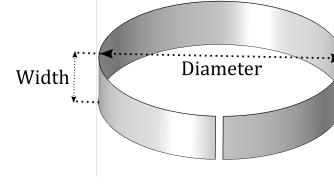


Figure 5: Basic helix  
width = 0.02 m and diameter = 0.08 m

partition generating an open surface. Furthermore, the height along the revolutions remains constant.

Argumentation of this definition:

It is obvious that the maximum revolution of the basic helix lies just under  $2\pi$  in order for it to remain an open surface. The minimum length is still open for interpretation. It can be argued that the minimum length could be anywhere between just below the maximum and zero. However, by choosing to reduce the revolution to anything less than just below  $2\pi$  questions whether it can be considered a helical surface at all.

## 2.2 Manual parametric optimization

This section will look into how the compliance properties change of the basic helix due to the introduction of curvature. However, before doing so, one first needs to have a method that breaks down translational and rotational compliance into comparable units. Here the Unified stiffness method by Leemans will be utilized. After this unification a metric is introduced to compare the change in compliance properties due to the changed geometry. In addition to this the second moment of area will be used to explain the reasoning behind the introduction of curvature and an overview of the iteration process will be presented. For clarification purposes the following table is presented providing an outline of the contribution for each section.

Section	Contribution
2.2.2	Leemans [16]
2.2.3	Author and Leemans [16]
2.2.4	Author
2.2.5	Author
2.3	Author

Table 1: Contribution overview

In order to preserve consistency and to have similar order of magnitude all of the helical geometries have a width equal to 0.02 m, a radius of 0.04 m and a thickness of 0.002 m. The



material model will be the same for all flexure mechanisms, namely a linear elastic isotropic **PolyLactic Acid (PLA)**.

### 2.2.1 Eigenscrew decomposition

Using Plücker coordinates, a displacement in three-dimensional space can be expressed in terms of linear and angular displacements in the form of a twist vector  $\vec{T}$ .

$$\vec{T} = \begin{bmatrix} \vec{\delta}_i \\ \vec{\gamma}_i \end{bmatrix} = \begin{bmatrix} (\vec{r}_i \times \vec{\gamma}_i) + h_i \vec{\gamma}_i \\ \vec{\gamma}_i \end{bmatrix}, \quad i = 1, 2, 3 \quad (7)$$

Here the upper half of the  $6 \times 1$  vector in equation 7 can be split into two parts. The first part consisting of a multiplication of angular displacement with the location vector  $\vec{r}_i$  while also being perpendicular to the direction of rotation  $\vec{\gamma}_i$ . The second part is parallel to the rotation and is depended on the scalar pitch  $h_i$ .

Along similar analogy, forces and moments can be expressed as a wrench vector  $\vec{w}$ .

$$\vec{w} = \begin{bmatrix} \vec{f}_i \\ \vec{\tau}_i \end{bmatrix} = \begin{bmatrix} \vec{f}_i \\ (\vec{b}_i \times \vec{f}_i) + d_i \vec{f}_i \end{bmatrix}, \quad i = 1, 2, 3 \quad (8)$$

In this case the lower half of the  $6 \times 1$  vector in equation 8 i.e. the moment couples can be split into two parts. The first part being a multiplication of the linear force with the location vector  $\vec{b}_i$  and is perpendicular to the direction of the force  $\vec{f}_i$ . The second part is parallel to the force and is depended on the ratio of angular torque to linear force  $d_i$ .

The compliance matrix (**C**) of a specific **Point Of Interest (POI)** expresses the constitutive relationship between the forces and displacement whereas the stiffness matrix (**K**) does it the other way around i.e. between displacements and forces:

$$\vec{T} = \mathbf{C} \vec{w} \quad (9)$$

$$\vec{w} = \mathbf{K} \vec{T} \quad (10)$$

**C** and **K** are the  $6 \times 6$  compliance and stiffness matrices. Note, that in a linear analysis the secant and tangent stiffness matrices are equivalent; hence from this point onwards these shall be referred to as the general compliance

and stiffness matrices.

Both **C** and **K** matrices can be transformed into an eigen-system described by Lipkin & Patterson [18] and shown below.

$$\mathbf{C} = [\hat{T}_f \quad \hat{T}_\gamma] \begin{bmatrix} a_f & 0 \\ 0 & a_\gamma \end{bmatrix} \begin{bmatrix} \hat{T}_f \\ \hat{T}_\gamma \end{bmatrix} \quad (11)$$

$$\mathbf{K} = [\hat{w}_f \quad \hat{w}_\gamma] \begin{bmatrix} k_f & 0 \\ 0 & k_\gamma \end{bmatrix} \begin{bmatrix} \hat{w}_f \\ \hat{w}_\gamma \end{bmatrix} \quad (12)$$

The eigenscrew decomposition describes both the three translational as well as the three rotational principle axes. In addition to direction, this decomposition also provides stationary multiplier values for each of these directions. Here the multipliers  $k_{fi}$  are the translational stiffnesses in the directions of the  $\vec{f}_i$  and  $k_{\gamma i}$  are the angular stiffnesses in the directions of  $\vec{\gamma}_i$ . The translational compliance is the inverse of  $k_{fi}$  and in a similar manner the rotational compliance is the inverse of  $k_{\gamma i}$ , see equations 13 and 14 below.

$$a_{fi} = \frac{1}{k_{fi}} \quad (13)$$

$$a_{\gamma i} = \frac{1}{k_{\gamma i}} \quad (14)$$

Equation 15 represents the eigenwrenches as well as the directional axis of these wrenches.

$$\mathbf{w}_{fi} = \begin{bmatrix} \vec{f}_i \\ \vec{\tau}_i \end{bmatrix}, \quad i = 1, 2, 3 \quad (15)$$

Applying an eigenwrench  $\mathbf{w}_{fi}$  leads to an induced twist  $\mathbf{T}_{fi}$ . The induced twists are pure translational and parallel to the eigenwrench.

$$\mathbf{T}_{fi} = \begin{bmatrix} a_{fi} \vec{f}_i \\ 0 \end{bmatrix}, \quad i = 1, 2, 3 \quad (16)$$

Equation 17 represents the eigentwist as well as the directional axis of these twists.

$$\mathbf{T}_{\gamma i} = \begin{bmatrix} \vec{\delta}_i \\ \vec{\gamma}_i \end{bmatrix}, \quad i = 1, 2, 3 \quad (17)$$

Applying an eigentwist  $\mathbf{T}_{\gamma i}$  leads to an induced wrench  $\mathbf{w}_{\gamma i}$ . The induced wrenches are pure couples parallel to the eigentwists.

$$\mathbf{w}_{\gamma i} = \begin{bmatrix} 0 \\ k_{\gamma i} \vec{\gamma}_i \end{bmatrix}, \quad i = 1, 2, 3 \quad (18)$$

The eigentwists and eigenwrenches in equations 11 and 12 are normalized such that the linear force and angular displacement have unit magnitude.

In summary, this eigenscrew decomposition treats the kinematic information within the compliance matrix as screws. Screw theory allows one to differentiate between the lines along a force that yield a parallel translation and a rotation that yields a parallel moment [5]. These lines are referred to as eigenwrenches and eigentwists.

### 2.2.2 Unification method

Screw theory so far has provided the means to describe the principle axes of a compliant mechanism. However, the diagonal matrices in equations 11 and 12 do not have consistent units. The stationary multipliers  $a_f$  in equation 11 have units of length per force parallel to the wrench axis. On the other hand, the stationary multipliers  $a_\gamma$  serve as the rotational compliance having units of angle divided by force multiplied by a length, expressed as a rotation around the twist axis. In order to solve this problem the **Rotation as an equivalent Translation (RasT)** approach by Leemans will be utilized [16].

Using virtual loads the RasT unification approach expresses rotational compliance as an equivalent translational compliance at the point of interest using solely forces to create a displacement. Furthermore, this approach is intuitive and is responsible for the coupling of the rotations and translations by including a twist pitch. The following section will explain the significance of the end result and how it transforms the stationary multipliers in comparable units. For further details of the exact derivations consult the work of Leemans [16].

In order to express a rotation as an equivalent translation, a unification length  $\chi_i$  is required, see equation 19 and 20.

$$\tilde{a}_{fi} = \chi_i^2 a_{\gamma i} \quad (19)$$

$$\chi_i = \sqrt{|r_i|^2 + h_i^2} \quad (20)$$

Using this unification variable one can express the rotational compliance as an translational equivalent  $\tilde{a}_{fi}$ .

$$\tilde{a}_{fi} = (|r_i|^2 + h_i^2) a_{\gamma i} \quad (21)$$

Along similar but opposite analogy one can express the rotational stiffness as an translational equivalent  $\tilde{k}_{fi}$ .

$$\tilde{k}_{fi} = \frac{k_{\gamma i}}{(|r_i|^2 + h_i^2)} \quad (22)$$

The point has arrived where the diagonal matrices in equation 11 and 12 containing the stationary multiplier values can be substituted with  $\tilde{\mathbf{a}}_f$  (equation 23) and  $\tilde{\mathbf{k}}_f$  (equation 24). One should realise that now  $\tilde{\mathbf{a}}_f$  has units of length per force and no rotational compliance;  $\tilde{\mathbf{k}}_f$  solely has units of force per length and also no rotational stiffness.

$$\tilde{\mathbf{a}}_f = \begin{bmatrix} a_{fi} & 0 \\ 0 & (|r_i|^2 + h_i^2) a_{\gamma i} \end{bmatrix} \quad (23)$$

$$\tilde{\mathbf{k}}_f = \begin{bmatrix} k_{fi} & 0 \\ 0 & \frac{k_{\gamma i}}{(|r_i|^2 + h_i^2)} \end{bmatrix} \quad (24)$$

The resulting equations for the compliance (**C**) and stiffness (**K**) matrices using the unified eigen-decompositions are described below.

$$\mathbf{C} = [\hat{T}_f \quad \hat{T}_\gamma] \begin{bmatrix} I & 0 \\ 0 & \frac{1}{\sqrt{|r_i|^2 + h_i^2}} \end{bmatrix} \tilde{\mathbf{a}}_f \begin{bmatrix} I & 0 \\ 0 & \frac{1}{\sqrt{|r_i|^2 + h_i^2}} \end{bmatrix} \begin{bmatrix} \hat{T}_f \\ \hat{T}_\gamma \end{bmatrix} \quad (25)$$

$$\mathbf{K} = [\hat{w}_f \quad \hat{w}_\gamma] \begin{bmatrix} I & 0 \\ 0 & \sqrt{|r_i|^2 + h_i^2} \end{bmatrix} \tilde{\mathbf{k}}_f \begin{bmatrix} I & 0 \\ 0 & \sqrt{|r_i|^2 + h_i^2} \end{bmatrix} \begin{bmatrix} \hat{w}_f \\ \hat{w}_\gamma \end{bmatrix} \quad (26)$$

Now all of the terms in the 6×6 compliance matrix have directly comparable units. This allows one to easily determine the dominant principle compliance directions of a flexure mechanism. This can also be done for the 6×6 stiffness matrix since all of its components have equivalent units.

### 2.2.3 Compliance metric

After consultation of the unified stiffness method it is now possible to define a metric. This performance measure provides meaningful insight

into the compliance characteristics of the selected flexure mechanisms. This ratio is a division where the numerator represents the individual 6 different compliance directions and the denominator represents the smallest compliance value of the 6 principle directions.

$$C_j = \frac{C_{direction_j}}{C_{smallest}}, j = 1, 2, \dots, 6 \quad (27)$$

The different helical geometries will be compared according to this assessment metric.

#### 2.2.4 Adding curvature via general equations

Taking the basic helix in section 2.1.3 as a starting point we propose to change how material is distributed w.r.t a particular axis. This is achieved by using a geometric property known as the second moment of area or area moment of inertia [19].

Firstly, one requires to locate the centroid of a shape using the first moment of area. The centroid is important because it shows the location of the neutral axis, a plane where no strain upon bending exists [19]. For symmetrical homogeneous bodies, the centroid is located at the geometric center.

Secondly, curvature shall be introduced to the cross-section of basic helix in the form where  $c \neq 0$ , hence additional terms will be added resulting in equations 28, 29 and 30 below. This will change how material is distributed along the orthogonal axis.

$$x = x(u, v) = \left( a + c \cos \frac{n\pi v}{d} \right) \cos(u) \quad (28)$$

$$y = y(u, v) = \left( a + c \cos \frac{n\pi v}{d} \right) \sin(u) \quad (29)$$

$$z = z(u, v) = b u + v \quad (30)$$

To start off, figure 6a represents the cross section of a leaf spring. The YZ axis is fixed and the centroidal axis is represented by  $y_c$  and  $z_c$ . Note, that in this case the fixed coordinate system is equivalent to the centroidal axis. Equations 31 and 32 show how the second moment of area ( $I_Y$  and  $I_Z$ ) is calculated.

$$I_Y = I_{y_c} = \int_{-\frac{w}{2}}^{\frac{w}{2}} \int_{-\frac{t}{2}}^{\frac{t}{2}} y^2 dy dz = \frac{w t^3}{12} \quad (31)$$

$$I_Z = I_{z_c} = \int_{-\frac{w}{2}}^{\frac{w}{2}} \int_{-\frac{t}{2}}^{\frac{t}{2}} z^2 dy dz = \frac{w^3 t}{12} \quad (32)$$

Looking closer at these equations one can observe that the thickness 't' affects the moment area of inertia around the y-axis in a cubic manner. Similarly, the width 'w' dominates the second moment of area around the z-axis in a cubic fashion. In other words, when the leaf flexure is wide and thin ( $w \gg t$ )  $\rightarrow I_Z \gg I_Y$  and vice versa when the leaf flexure is narrow and thick ( $w \ll t$ )  $\rightarrow I_Z \ll I_Y$ .

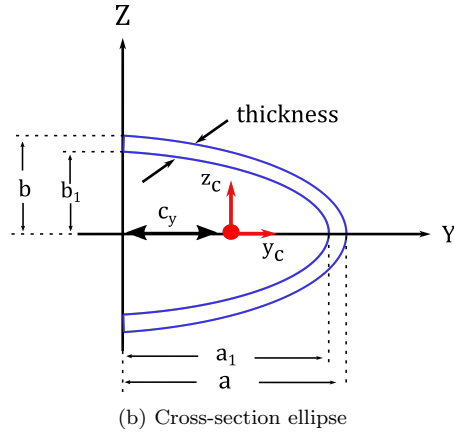
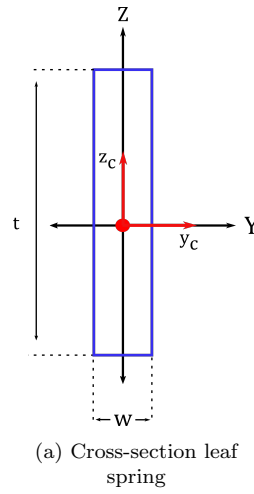


Figure 6: Cross-sections of rectangle and hollow half ellipse

In order to explain what happens to the area moment of inertia due to the introduction of curvature, the cross-sectional shape of an hollow half ellipse was chosen (see figure 6b). Here the parameters a and b determine the geometric properties of this half-hollow ellipse. Note, that  $a_1$  and  $b_1$  were chosen such

that the thickness always remains equal to 2 mm.

The area moment of inertia of a hollow half ellipse is calculated in a similar manner to the cross-section of the leaf spring. It also consists of first locating the centroid using the first moment of area. The centroid lies at the location  $(C_y, C_z)$ . However, for this geometry it is easier to calculate the second moment of area around the fixed YZ orthogonal axis (see equations 35 and 37) and not around the centroid as was done for the leaf spring calculations.

$$Area = \frac{\pi}{8} (ab - a_1b_1) \quad (33)$$

$$C_y = \frac{a + a_1}{4}, \quad C_z = 0 \quad (34)$$

The parallel axis theorem can then be used to correct the area moment of inertia such that it only looks at the centroid. It does so by subtracting the product of the shapes area and the square of the perpendicular distance between these axes [19]. Equations 36 and 38 make use of this theorem.

$$I_Y = \frac{\pi (ab^3 - a_1b_1^3)}{8} \quad (35)$$

$$I_{yc} = I_Y - Area \times C_z^2 \quad (36)$$

$$I_Z = \frac{\pi (a^3b - a_1^3b_1)}{8} \quad (37)$$

$$I_{zc} = I_Z - Area \times C_y^2 \quad (38)$$

Similar to the moment area of inertia for the leaf spring, when the half ellipse has a relative large amplitude ( $a \gg b$ )  $\rightarrow I_{zc} \gg I_{yc}$  and vice versa when the half ellipse has a relative small amplitude and is wide ( $a \ll b$ )  $\rightarrow I_{zc} \ll I_{yc}$ . Figure 7 shows a plot of the second moment of area against the ellipse height.

For demonstration purposes  $a = b$  but it is noticeable that the larger the ellipse height, the larger the area moment of inertia for both y and z directions. Area moment of inertia is higher in the  $y_c$  - direction due to the location of the centroid not being the same as the fixed

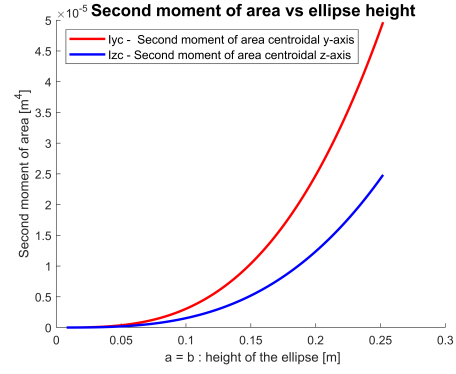


Figure 7: Second moment of area vs increasing height

coordinate system.

According to the theory of elastic bending, second moment of area influences the stiffness. Equations 39 and 40 state how the dimensions are related to each other, with M - internal moment, I - second moment of area, E - Young modulus, R - radius,  $\sigma$  stress, y - linear distance from neutral axis and  $\kappa$  - curvature.

$$\frac{M}{I} = \frac{E}{R} = \frac{\sigma}{y} \quad (39)$$

$$M = EI\kappa \quad (40)$$

Increasing the second moment of area requires a larger bending moment to achieve the same deflection. In other words, the stiffness increases.

## 2.2.5 Overview of iteration process

This section introduces the chosen helical flexure geometries. A pictorial overview of helical flexure shapes with key geometrical properties has been provided in table 2. The first column indicates the helix number. The second column represents visual impressions of the helical flexure models. The blue line  $\Omega$  indicates where the mechanism is fully constraint and the red line P shows where the mechanism is actuated at the POI. The third column provides information regarding the geometric properties.

The last model geometry (Helix 6) of table 2 was selected for further investigation. In the next section more details shall be provided involving the principle directions allowing a deeper insight into the kinematic capabilities of this complaint mechanism.

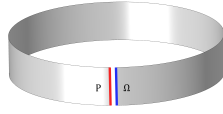
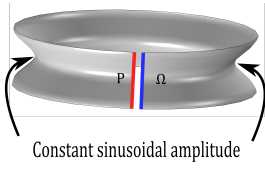
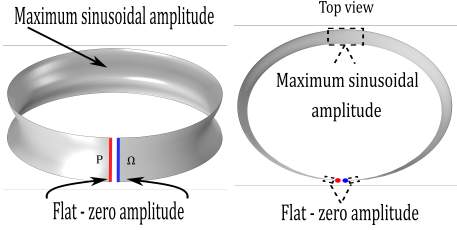
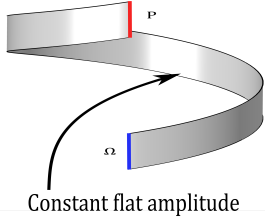
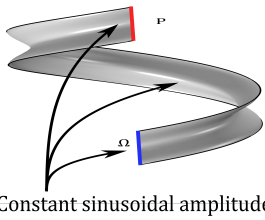
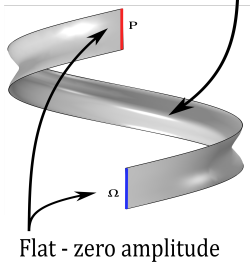
Helix number	Model	Geometric properties
Helix 1		Basic helix $c = 0, d \gg 2\pi b \gg 1$ Constant flat amplitude
Helix 2		$c \neq 0, n = 2, d \gg 2\pi b \gg 1$ Constant sinusoidal amplitude
Helix 3		$c \neq 0, n = 2, d \gg 2\pi b \gg 1$ Non-constant sinusoidal amplitude Maximum at $\pi$ Minimum i.e. 0 amplitude at $0\pi$ and $2\pi$
Helix 4		$c = 0, n = 2, d \ll 2\pi b \ll 1$ Constant flat amplitude Increasing height along revolution
Helix 5		$c \neq 0, n = 2, d \ll 2\pi b \ll 1$ Constant sinusoidal amplitude Increasing height along revolution
Helix 6		$c \neq 0, n = 2, d \ll 2\pi b \ll 1$ Non-constant sinusoidal amplitude Maximum at $\pi$ Minimum i.e. 0 amplitude at $0\pi$ and $2\pi$ Increasing height along revolution

Table 2: Pictorial overview of helical flexure elements with the key geometrical properties

## SCH Flexure

Using screw theory it is possible to locate the six principle axes and their corresponding magnitudes. Some magnitudes are too small to visualize. Therefore, the first set of figures will show the principle directions without magnitude. This is followed by a more detailed zoom in figure illustrating magnitude.

This shell mechanism is analysed as an **IsoGeometric Analysis (IGA)** shell, a software developed at the Delft University of Technology. It has the following dimensions and material properties: thickness 0.002 m, Young Modulus 3.5 GPa [23] and a Poisson ratio of 0.45 [23]. This geometry is described by a **Non-Uniform Rotational B-Splines (NURBS)** surface tool [20], a third polynomial following a  $3 \times 10$  grid. The values of this polynomial take a special form tailored for the IGA software.

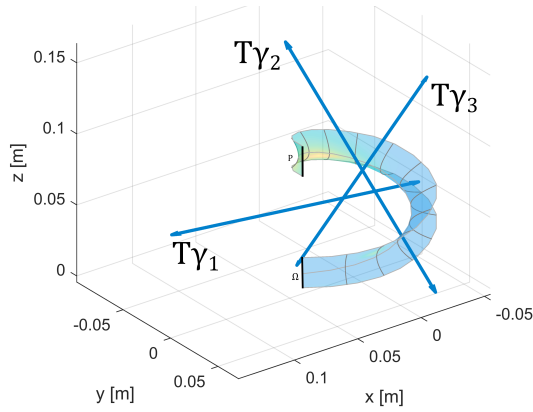


Figure 8: Twist axes with no stationary multipliers

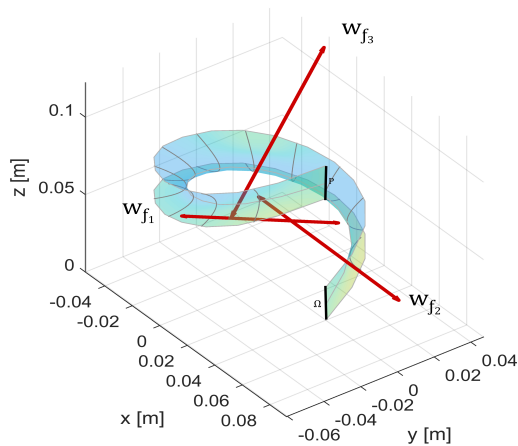


Figure 9: Wrench axes with no stationary multipliers

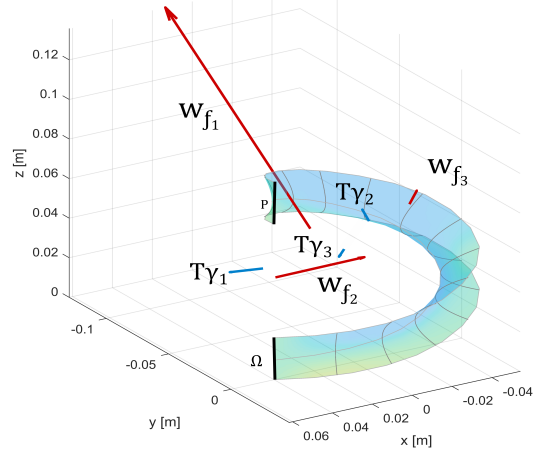


Figure 10: Unified stiffness with stationary multipliers

Figure 8 shows the directions of the eigentwists with no stationary multipliers. Similarly, figure 9 shows the directions of the eigenwrenches with no stationary multipliers. Furthermore, figure 10 shows the directions and magnitude of the unified stiffness. All of the stationary multipliers have comparable units.

$$w_{f1} > w_{f2} > T_{\gamma1} > T_{\gamma2} > T_{\gamma3} > w_{f3} \quad (41)$$

Figure 10 and equation 41 show that the lowest compliance vector, its inverse being the largest stiffness, corresponds to wrench  $w_{f1}$ .

## 2.3 Application: 3DoF stage

In this section the SCH flexure element (Helix 6) in figure 10 shall be used to synthesize a complaint motion stage. The FACT method [4] will be implemented. However, before doing so an important assumption will be made. We propose to model the largest constraint direction  $w_{f1}$  in the SCH flexure element (figure 10) as a single wrench constraint. This wrench constraint also known as a **Degree of Constraint (DoC)** is not pure i.e. there is coupling. The other directions will be treated as degrees of freedom essentially making the SCH flexure a 5 DoF mechanism. The following provides a visual representation of the constraint and freedom space.

Here the orange line on the left side of figure 11 represents the constraint space as a single wrench that is collinear with the desired screw DoF. Its coupled moment to force ratio  $-q$ , equals pitch  $p$ . The green line on the right side of figure 11 corresponds to the screw motion. This freedom space features (i) screws with a

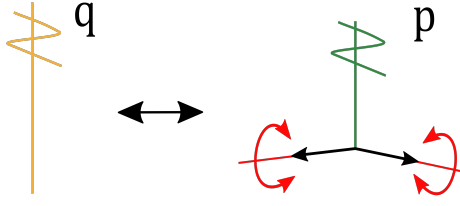


Figure 11: Constraint and freedom space SCH flexure element

pitch of  $p$  that lay on planes that intersect the screw axis, (ii) rotations and screws that lay on the surfaces of circular hyperboloids and (iii) translations that are perpendicular to the screw axis [21].

Now three elements will be used to generate a flexure system consisting of three DoF: a screw and two orthogonal translations. The freedom space is made up of (i) a box of screws that are parallel to the axis of the desired screw (ii) a plane of translation arrows that are orthogonal to the screw axis. Consequently, the freedoms complementary constraint space exhibits (i) a box of wrenches parallel to the screw axis and (ii) a disk of pure moments normal to the screw axis. Furthermore, two wrenches that are co-planner constrain a rotation in that plane. This results into the following constraint (figure 12) and freedom spaces (figure 14).

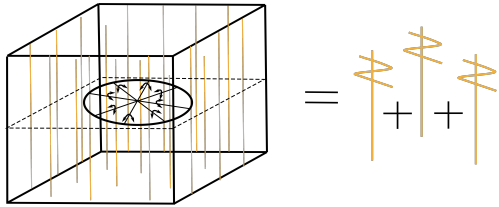


Figure 12: Constraint topology

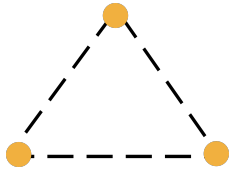


Figure 13: Constraint topology top view

We are now in a position where the helical motion stage can be assembled. The SCH flexure in figure 10 is rotated such that its dominant constraint points vertically upwards. Attaching 3 SCH flexures 120 degrees apart and equally

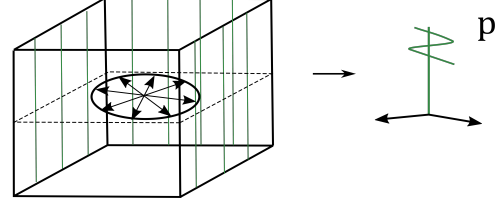


Figure 14: Freedom topology

spaced produces the previously mentioned freedom and constraint topologies. Hence, the following motion stage is presented:

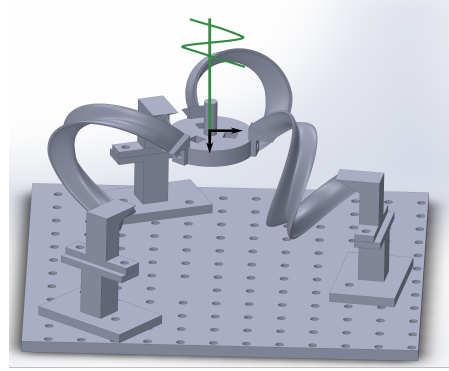


Figure 15: Three DoF stage with three SCH flexures

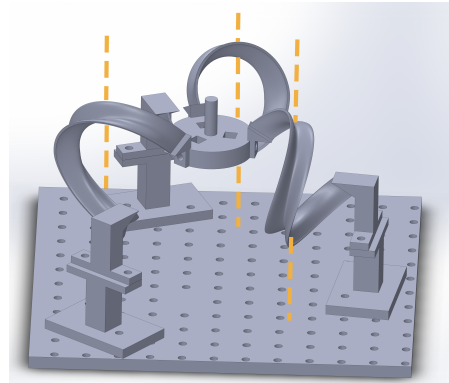


Figure 16: Three wrench constraints

### 3 Results

This section will present the compliance metric of the different helical surfaces. This is followed by performing an eigenfrequency analysis of the helical motion stage using Comsol. Lastly, this numerical modal is experimentally validated with an eigenfrequency vibration test.



### 3.1 Metric

Table 3 provides a metric overview of the modelled principle directions split by type of screw for different helical flexure shapes.

Helical Flexure Shape	Type of Screw					
	Wrench			Twist		
	Principle Directions ( $C_j$ )					
	$C_1$	$C_2$	$C_3$	$C_4$	$C_5$	$C_6$
Helix 1	6.5	11	12	1.0	16	33
Helix 2	1.3	1.0	25	2.6	37	4.0
Helix 3	1.8	3.4	16	1.0	12	2.3
Helix 4	1.0	2.0	2.3	1.8	3.1	6.1
Helix 5	1.0	2.3	12	8.0	21	7.0
Helix 6	1.0	3.0	18	3.5	8.0	12

Table 3: Compliance metric

Each helix in every row has a ratio equal to one. This represents the direction having the lowest compliance. All the other values represent how much more compliant that particular direction is w.r.t. the lowest compliance multiplier.

### 3.2 Numerical model

A **Finite Element Model (FEM)** analysis was performed using Comsol Multi-physics. The CAD model was constructed in SolidWorks and imported into the Comsol platform. The helical flexures were modelled using shell elements since this reduces the required computational power. Similar to what was used for dimensions and material properties in the IGA software, the thickness is 0.002 m, Youngs Modulus 3.5 GPa [23] and a Poisson ratio of 0.45 [23]. The following table shows the first 6 Comsol modelled eigenfrequencies and their corresponding mode shapes.

Eigenfrequency	Comsol [Hz]	Mode shape [Translation/Rotation]
1 <sup>st</sup>	26.5	$T_x$
2 <sup>nd</sup>	26.5	$T_y$
3 <sup>rd</sup>	40.0	Screw: $R_z$ , $T_z$
4 <sup>th</sup>	49.0	$R_x$
5 <sup>th</sup>	49.0	$R_y$
6 <sup>th</sup>	70.5	Screw: $R_z$ , $T_z$

Table 4: Numerical eigenfrequencies and mode shapes

### 3.3 Experiment

To verify the outcomes that resulted from FACT and FEM analysis, the following experiment was conducted. A prototype of the proposed 3DoF motion stage has been made by additive manufacturing of PLA. The individual parts have been fabricated separately and joined together using bolts and nuts. Rather than measuring the motion and constraint directions with a displacement inducer, the eigenfrequencies have been measured with a modal vibration test. Installing the stage on a vibration isolation table and exciting it with an impact hammer allows one to measure the vibrations present in the flexure system. This was done using a single laser Doppler sensor (Polytec OFV505), which measures the velocity of the end-effector. The velocity-time signal is read out by a controller unit (OFV2200) and is then converted from analog to digital using a NI USB-6006 DAQ device. Furthermore, the digital velocity-time signal is transformed to the frequency domain using the **Fast Fourier Transform (FFT)** function available in the Matlab software. To make sure that all vibrational modes are measured the end-effector is excited at multiple positions. Additionally, the Doppler sensor has been moved around such that the laser points at different locations of the end-effector. See figure 17 below for the experimental set up.

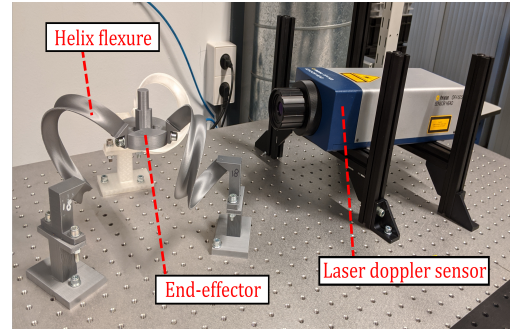


Figure 17: Experimental set up

Figure 18 shows the frequency response spectrum of the conducted experiment. The red dots at the top of the peaks, which indicate the eigenfrequencies, have been added for visual aid. The eigenfrequencies have been recorded in table 5 below. The third column of this table shows how much the experimental and numerical eigenfrequencies differ from each other.



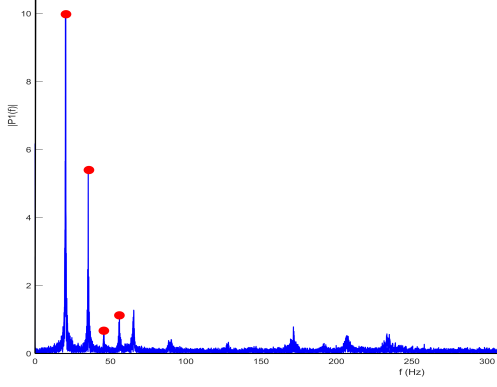


Figure 18: Frequency response spectrum

Eigenfrequency	Experiment [Hz]	Difference experiment
1 <sup>st</sup>	20.4	29.0%
2 <sup>nd</sup>	-	-
3 <sup>rd</sup>	35.0	14.0%
4 <sup>th</sup>	45.0	8.0%
5 <sup>th</sup>	-	-
6 <sup>th</sup>	65.0	8.0%

Table 5: Eigenfrequencies experiment

Note, that in the experiment it was not possible to differentiate between the 1<sup>st</sup> and 2<sup>nd</sup> eigenfrequency. This was also the case for the 4<sup>th</sup> and 5<sup>th</sup> eigenfrequency. This can be explained due to the symmetrical design of the flexure system leading to degeneracy of the eigenfrequencies. The second part 'Motion stage' in section 4 will provide further explanation.

## 4 Discussion

The main research objective of this paper focusses on the implementation of spatial flexures in motion stages. This main objective is split into two parts. The first one looks into the understanding of helical flexure geometries with varying curvature. The second part is to more specifically use a helical flexure element and to build, using such an element, a 3DoF compliant motion stage. The results and outcomes of each contribution will be discussed and analysed.

### Flexure design

Using differential geometry it is possible to describe the mathematical surface of a helical geometry. The choice was made to further pursue the family of helical surfaces with a sinusoidal generatrix. Starting from the basic helix, complexity was introduced via the addition of curvature. This was done with the intent of changing the second moment of area which influences the compliance properties of the helical flexure. Then using screw theory and the unified stiffness method a performance metric was created. This provided insight into the properties of various helical flexure geometries. The metric shows how the most dominant constraint changes after the introduction of curvature. For instance, the most basic helix (helix 1) is stiff along rotation  $T_{\gamma 1}$  but is relatively compliant around  $T_{\gamma 3}$ . This is explained by the fact that the width is orders of magnitude larger than the thickness. After introducing a sine-wave along the cross-section, the compliance properties change. Helix 2 is more stiff along  $w_{f1}$  and  $w_{f2}$ , while  $w_{f3}$  has become relatively more compliant. This helix is also less rotationally compliant along the direction of  $T_{\gamma 1}$ . These observations can be explained by the change of the area moment of inertia, where both in plane stiffness directions have increased. Furthermore, the SCH flexure (helix 6) is stiff along the direction of  $w_{f1}$  but has relatively more compliance along the direction of  $w_{f3}$ . However, given the nature of these spatial structures, where the stiffness ratios have a similar order of magnitude, it can be expected that the DoF and DoC lie close to each other.

It has been demonstrated that adding curvature to the cross-section of an helical surface influences its compliance characteristics. The addition of curvature is a possible explanation for what is observed in the SCH flexure (helix 6 in table 2). A high moment area of inertia around the Y and Z axes creates additional stiffness in those directions while one wrench remains relatively more compliant. The fact that this flexure is an open surface provides compliance that enables it to move out of the YZ-plane.

## Motion stage

Applying the acquired insights about helical flexure geometries led to the design of a helical complaint motion stage. An important assumption was made, namely, that the most dominant constraint is treated as a constraint direction leaving 5 freedom directions. This assumption allows the usage of FACT as a design method. In order to validate the conceptual design a FEM model was assembled using Comsol multiphysics. An eigenfrequency analysis was performed to get insight into the eigenfrequencies and their corresponding mode shapes. The first two modes shapes at roughly 26 [Hz] were both translations: one in x and the other in the y direction. The numerical eigenfrequencies show that these two values are very close to each other. This can be explained due to the 'perfect' symmetrical design leading to degeneracy of the eigenfrequencies [22]. The eigenmodes are still unique and are rotated with respect to one another. In theory, if one helical flexure has a different thickness or length essentially making the design less symmetrical, the eigenfrequencies should shift further away from each other. Furthermore, the third eigenfrequency at 40 [Hz] resembled a mode shape indicating the desired screw DoF. The mode shapes provide verification that the proposed helical motion stage is able to follow the intended freedom directions. However, the eigenfrequency analysis indicates that the two permitted translations are not pure translations as they do not entirely remain in plane. This is unwanted and considered as parasitic error. However, we believe that, given the symmetry in the system, the coupling is minimized by reasoning that the individual helical flexure elements, to some extent, cancel each other out. Moreover, by only looking at small-displacements the error is considered to be minimal but still present. Further research is required to determine the magnitude of this error.

Verification of the numerical model was obtained by experimentally measuring the eigenfrequencies with a modal vibration test. The data shows that the experimental eigenfrequencies are within a range of 8 to 29 percent of the numerical eigenfrequencies. Although the experiment match the data from the numerical model, ideally one would like to see the first parasitic eigenfrequencies to have a much higher value. The higher value will help the parasitic eigenfrequencies to be further apart and allow for better distinction between motion and

constrain directions. Furthermore, the experimental data cannot differentiate between the 2 eigenmodes sharing a similar eigenfrequency. The frequency response plot will therefore show one peak at similar eigenfrequency somewhat limiting comparison with those obtained in the numerical model.

There are also a number of other reasons for the difference between the numerical model and the experiment.

- (i) The difference between numerical and experimental eigenfrequencies could be due to inherent fabrication uncertainty of the 3D printed flexures.
- (ii) The FEM model of the helical flexure geometries also had a particular thickness. The eigenfrequencies have shown to be sensitive towards this thickness parameter as the stiffness scales with the cubic power.
- (iii) Error is introduced in assembling the helical flexures and end-effector of the stage. This results in possible miss-alignments of the principle directions. Any miss-alignments will lead to extra unwanted parasitic error. A monolithic fabrication might solve this challenge.
- (iv) Nuts and bolts were used to connect the different components to each other. This adds additional weight to the end-effector that also influences the numerical eigenfrequencies.
- (v) Clamping also affects the eigenfrequencies of the system. In the numerical model, these constraints were treated as fixed and thus are approximated as completely rigid. In reality, the support clamps that connect the ground with the helical flexure element has some finite stiffness affecting the numerical eigenfrequencies.
- (vi) Literature shows that the Young modulus of a printed material varies with printing direction [23]. These variations occur due to the presence of air gaps in the printed structure and stress concentration along filament beads [24]. Hence, the material properties of the printed helical flexures are far from being ideally isotropic.

## 5 Conclusion

In this paper, a systematic approach was implemented with the objective of guiding a stage using compliant helical flexure elements. Insight into the linear kinematic behaviour of various helical surfaces with varying curvature is provided with the usage of parametric optimization, screw theory, unified stiffness method and a performance metric. The newly acquired insights served as a prerequisite for selecting a suitable topology capable of guiding a stage. Additionally, an eigenfrequency analysis was performed and experimentally validated with a model vibration test. This led to the successful realization of a helical based compliant motion stage. An outcome of this study provides evidence that complex spatial flexure geometries can be utilized in such a way that they become practically relevant in the world of precision positioning systems.

## References

- [1] S. Sen, *Beam Constraint Model: Generalized Nonlinear Closed-form Modeling of Beam Flexures for Flexure Mechanism Design*. PhD thesis, University of Michigan, 01 2013.
- [2] L. Howell, *Handbook of Compliant Mechanisms*. John Wiley and Sons, 02 2013.
- [3] H. Soemers, *Design Principles for Precision Mechanisms*. T-Point Print VoF, 2010.
- [4] J. Hopkins, J. Vericella, and C. Harvey, “Modeling and generating parallel flexure elements,” *Precision Engineering*, vol. 38, 07 2014.
- [5] W. van de Sande and J. Herder, “Analysis of parasitic motion in compliant mechanisms using eigenwrenches and eigentwists,” *Journal of Mechanisms and Robotics*, p. V05AT07A020, 08 2018.
- [6] K. Gunnink, R. Aarts, and D. Brouwer, “Performance optimization of large stroke flexure hinges for high stiffness and eigenfrequency,” *ASPE*, 2013.
- [7] J. Rommers and J. Herder, “Design of a folded leaf spring with high support stiffness at large displacements using the inverse finite element method,” in *Advances in Mechanisms and Machine Science* (T. Uhl, ed.), Mechanisms and Machine Science, pp. 2109–2118, Springer, 2019.
- [8] J. Rommers, M. Naves, D. Brouwer, and J. Herder, “A large range spatial linear guide with torsion reinforcement structures,” in *ASME 2018 International Design Engineering Technical Conferences and Computers and Information in Engineering Conference*, vol. 5A, (United States), American Society of Mechanical Engineers (ASME), 1 2018.
- [9] J. Nijssen, *A Type Synthesis Approach to Compliant Shell Mechanisms*. PhD thesis, TU Delft, 01 2017.
- [10] S. Guest and S. Pellegrino, “Analytical models for bistable cylindrical shells,” *Proceedings of The Royal Society A: Mathematical, Physical and Engineering Sciences*, vol. 462, pp. 839–854, 03 2006.
- [11] C. K. A. Broshuis, J. Rommers and J. Herder, “Negative stiffness in compliant shell mechanisms,” 2019.
- [12] G. Radaelli and J. Herder, “Gravity balanced compliant shell mechanisms,” *International Journal of Solids and Structures*, 04 2017.
- [13] S. Walker and G. Aglietti, “An investigation of tape spring fold curvature,” 07 2004.
- [14] G. Radaelli and J. Herder, “Study on the large-displacement behaviour of a spiral spring with variations of cross-section, orthotropy and prestress,” *Mechanical Sciences*, vol. 9, pp. 337–348, 10 2018.
- [15] J. Nijssen, J. Herder, J. Ring, G. Radaelli, and C. Kim, “Spatial concept synthesis of compliant mechanisms utilizing non-linear eigentwist characterization,” 09 2018.
- [16] J. R. Leemans, C. J. Kim, W. W. P. J. van de Sande, and J. L. Herder, “Unified Stiffness Characterization of Nonlinear Compliant Shell Mechanisms,” *Journal of Mechanisms and Robotics*, vol. 11, 12 2018. 011011.
- [17] V. I. S.N. Krivoshapko, *Encyclopedia of Analytical Surfaces*. Springer, 2015.
- [18] H. Lipkin and T. Patterson, *Geometrical decomposition of robot elasticity*. IEEE, 10 1992.

- [19] R. Hibbeler, *Mechanics Of Materials*. Pearson, 2010.
- [20] W. T. L. Piegl, *The NURBS book*. Springer, 2012.
- [21] J. Hopkins, “A visualization approach for analyzing and synthesizing serial flexure elements,” *Journal of Mechanisms and Robotics*, vol. 7, p. 031011, 08 2015.
- [22] M. Geradin and D. J. Rixen, *Mechanical Vibrations: Theory and Application to Structural Dynamics, 3rd Edition*. Wiley, 2015.
- [23] Y. Zhao, Y. Chen, and Y. Zhou, “Novel mechanical models of tensile strength and elastic property of fdm am pla materials: Experimental and theoretical analyses,” *Materials and Design*, 2019.
- [24] K. Szykiedans, W. Credo, and D. Osinski, “Selected mechanical properties of petg 3-d prints,” *Procedia Engineering*, vol. 177, pp. 455 – 461, 2017.



# 3

## Discussion

This part provides recommendations and finishes with a general outlook highlighting the contribution of this thesis.

### Recommendations

We expect a growing demand for spatial compliant building blocks in the near future. It has yet to be determined through what medium spatial flexure elements are deemed most adequate. This thesis has provided insight and contribution by mapping out the linear kinematic behaviour of a sub-class of ordinary helical flexure geometries. More importantly, it offers a basis in terms of simplifying the complex nature as well as revealing fruitful future research directions paramount to the promotion of helical flexure elements. An essential reoccurring theme in this thesis was the fact that the compliance metric of the helical surfaces exhibited similar order of magnitude. This results in less-well defined freedom and constraint directions in comparison with flat flexure geometries such as present leaf springs. It is still uncertain whether it is mechanically possible to achieve similar stiffness ratios for this group of shell mechanisms. At least for the helical flexure geometries that were considered in this thesis it was not the case. However, there have been indications that helical surfaces might have a larger operating range and that the support stiffness over a RoM does not diminish as aggressively in comparison with 2D flexure elements. It must be stressed that this is a speculation and hence could be further investigated. Besides this, there are other potential interesting research directions. For instance, looking into the non-linear behaviour over a large RoM or performing a more critical analysis of the induced parasitic error. Another interesting direction would be to primarily consider helical elements that either alone or combined are able to follow a linear motion path i.e. a linear guide. Usually shell compliant mechanisms are not perfect translational or rotational systems and a pitch can often be expected. This was also observed with the studied helical flexure geometries. However, it might be possible, using symmetry or other smart solutions, to bypass these parasitic errors. Further research must be done to find out whether this can be accomplished, especially for a large RoM. Moreover, a large quantity of other helical surfaces exist. Each category may have interesting properties and applications that might be worthwhile for further investigation.

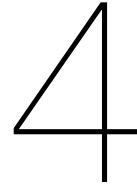
The following list provides additional research directions that could also lead to potentially useful insights.

1. *Center-of-compliance*: Actuation from the center of compliance of a flexure element results in pure translations and rotations. Further work is required on how to accomplish this for more complex shell elements.
2. *Optimization*: Some helical mechanisms may experience variations of the most dominant constraint due to large RoM. Optimization of these shell elements also requires further investigation.

3. *Spirals*: these surfaces might have properties that helical flexure geometries do not have. A direct comparison between the two in order to extract differences and similarities would be interesting.
4. *Hybrid topologies*: Combining 2D and 3D flexure building blocks in serial or parallel requires further investigation.
5. *Stiffness-ratios*: Further analysis on how to attain stiffness ratios for shell mechanisms that are similar to that of 2D flexures.
6. *Variable thickness and flexure width*: Given that stress distributions are not the same every it would be compelling to see the effect on, for instance, stiffness properties.

## Outlook

A successful effort was made to model a helical flexure element such that it is compatible for synthesizing multi-DoF flexure systems using FACT. In theory, this foundation building block can be used for many more FACT freedom and constraint topologies. Additional research is required to show that this is indeed the case. The addition of an elementary spatial building block that is also compatible with planar synthesis methods opens the door to many solutions that previously were not possible. Furthermore, the parametric equations describing these helical surfaces provides designers with the tools to shape it to their own specific needs. This thesis focuses on the introduction of curvature along the cross section, but this is just one aspect out of a very large pool of choices. Expanding this into a more diverse and accessible geometry library reduces the design barriers that exist and will promote the synthesis of using spatial elements in multi-DoF flexure systems.



## Conclusion

This work has presented a systematic approach with the objective of guiding a stage using compliant helical flexure elements. Merging the field of differential geometry with compliant mechanisms enables one to use the abundant literature on surface equations. This has led to a new and wide variety of spatial flexure elements that previously were not considered. Upon selection of a particular sub-class of helical flexure geometries, insight into the linear kinematic behaviour of various helical surfaces with varying curvature is provided. These insights served as a prerequisite for selecting a suitable topology and led to the successful realization of a helical based compliant motion stage. This thesis provides a basis for synthesising future motion stages using spatial elements as fundamental building blocks. Furthermore, this study has demonstrated that complex spatial flexure geometries can be utilized in such a way that they become practically relevant in the world of precision positioning systems.







## Appendix



# Contents

Appendices	1
A Helix 3D printing	1
B Helical flexure element design iterations	3
C Stage design iterations	5
D Comsol mesh sensitivity	7
E Sensitivity analysis of Comsol models	7
F Eigenmodes of Comsol model	8
G Comsol pitch calculations	11
H Symmetry of helical flexure stage	12
I Second moment of area	12
J Quantitative example - SCH flexure	16
K Unified stiffness and compliance visualization	19

## A Helix 3D printing

This appendix chapter provides a step-by-step method on how to create a helix using the parametric surface equations. It has been very time consuming to figure this out and 3D print a helix with a desired thickness. It shows how one can make an equation driven surface in Comsol Multi physics and import this geometry into a workable part that can be used in the SolidWorks part and assembly arena.

- first in Comsol:

Name	Expression	value	Description
a	0.04	0.04	Radius helix Factor
b	0.0125	0.0125	Width of the slab (factor)
c	0.008	0.008	Amplitude sin (factor)
k	1	1	Number of revolutions
NumRev	$2\pi k$	6.28	Number of rev multiples of $2\pi$
n	2	2	Amount of semi-whole waves
sb	0.27	0.27	Pitch height multiplier
d	$2 b sb \pi$	0.02	Corrugation curvature

- The analytic functions are available in Comsol to create a triangle function. This allows one to linearly alter the amplitude of the curvature along the corrugations.

- Using shell elements, it is possible to plug everything into the parametric surface equations, see figure 2. Note, that the  $pw1(u)$  is the piecewise function (2) transforming the sinusoidal amplitude.

- Build the geometry and then select Geometry, right-mouse click and export
- Under 'File type' select: Parasolid binary file (\*.x b;\*.xmt bin)
- Then select a place to save it under 'name.x\_b'
- Select entire finalized geometry.
- Uncheck split in manifolds

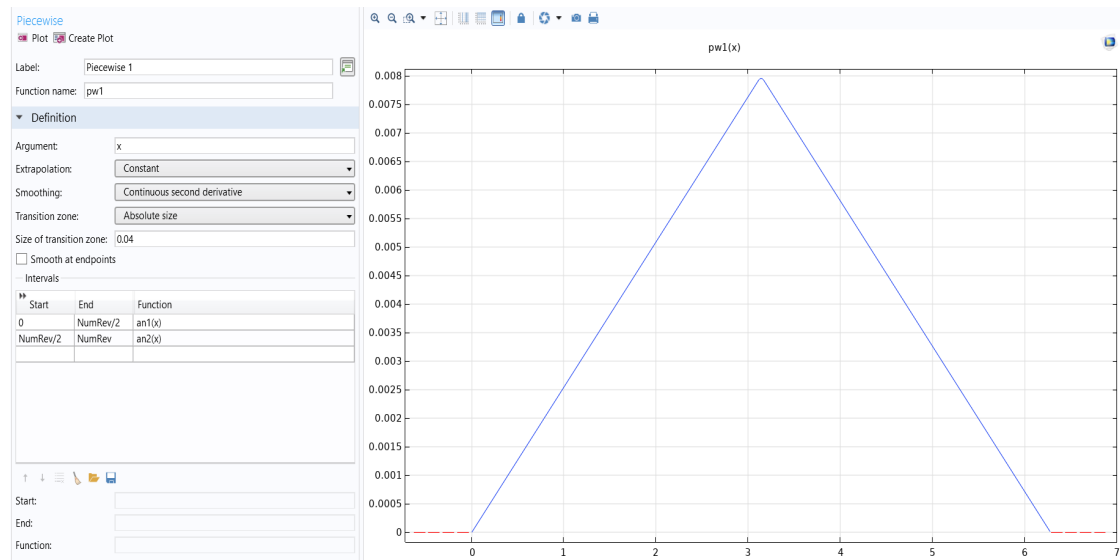


Figure 1: Piecewise continuous function

The screenshot shows the 'Parametric Surface' software interface. The 'Parameters' section has two parameters: 'u' and 'v'. The 'Expressions' section shows the parametric equations for x, y, and z. The 'Position' section shows the coordinates x, y, and z.

Label: Parametric Surface 1

**Parameters**

First parameter

Name: u

Minimum: 0

Maximum: NumRev

Second parameter

Name: v

Minimum: 0

Maximum: d

**Expressions**

x:  $(a + pw1(u) * \cos(n * v * \pi / d)) * \cos(u)$  m

y:  $(a + pw1(u) * \cos(n * v * \pi / d)) * \sin(u)$  m

z:  $(b * u) + v$  m

**Position**

x: 0 m

y: 0 m

z: 0 m

Figure 2: Parametric equations

- Select export

Then in SolidWorks:

- Go to File, select open. Then under quick filter select: Parasolid(\*.x\_t,\*.x\_b;\*.xmt\_txt\*,.xmt\_bin)
- Open the file with the name that was provided

Now the surface is in the SolidWorks area. Time to make it a 3 dimensional part.

- Insert → Boss/Base → Thicken
- Select the imported surface
- When choosing thickness play around with the 3 options: ticken above, below or both
- Using the 'both' thicken seems to work best

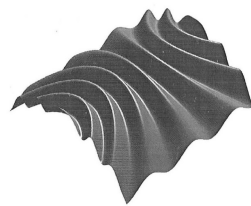
- select 1 mm for both → hence thickness is 2 mm.

Sometimes the edges of the helical surface is are not flat. Hence, one needs to cut them via a sketch plane. This is one way of doing it.

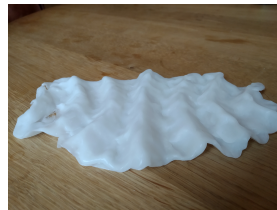
- Select a sketch plane at the beginning or end
- Draw a rectangular square
- Insert → surface → fill
- Insert → cut → thicken (this allows you to select the surface you just made and while also selecting a cutting range)
- After pressing the green tickbox, you get a window bodies to keep
- Press selected bodies and only select the helix
- Done

## B Helical flexure element design iterations

During the initial phase of the project there were some hand-on practical sessions where some shapes were construed out of clay and plastic in order to get a feel of how a structure deforms when subject to a load or displacement. These geometries looked interesting. Here are some images of that process.



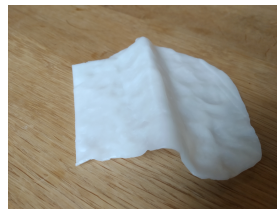
(a) Scallop Shell Norman



(b) Scallop Shell Top



(c) Scallop Shell Side



(d) Straight Corrugation

Figure 3: Design process 1

After the fabricating the scallop shell. It was proposed to further investigate how curvature changed the properties of the structure. Rather than looking at multiple corrugations the focus was directed at just one.



(a) Curved Corrugation



(b) Clay Model Front

Figure 4: Design process 2a



(a) Own Shape Back



(b) Own Shape Side

Figure 5: Design process 2b

Although these shapes did show some interesting properties. This did not lead to any fruitful results and was not investigated further. Another direction was chosen, namely helical surfaces.



(a) Helix flat top



(b) Helix flat side

Figure 6: Design process helix 2c



(a) Helix corrugated top



(b) Helix corrugated side

Figure 7: Design process helix 2d

First a helix with no sinusoidal amplitude was made (figure 6). From this curvature was intro-

duced to see how it influences the kinematic behaviour, see figure 7.



(a) Helix corrugated flat top



(b) Helix corrugated flat side

Figure 8: Design process helix 2e

After using clay, also many flexure concepts were printed to explore its kinematics. As it was difficult to visualize the kinematic behaviour. Many concepts were not used. For instance, the helix geometries of half a revolution. The did not provide the kinematics that were suitable for a motion stage design.



(a) Helical surfaces with curvature



(b) Half helix curvature

Figure 9: Design process helical surfaces 3a

Figures 10 show different clamping possibilities. The orientation of the clamping influences the overall stiffness characteristics. Eventually, it was chosen to clamp the final helical flexure in the orientation shown in figure 10b.



(a) Helix iteration 1



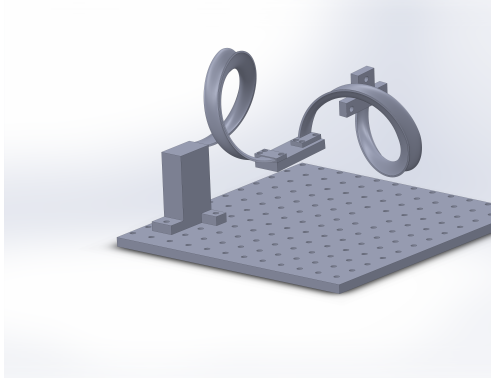
(b) Final SCH helix with clamp

Figure 10: Design process helical surfaces 3b

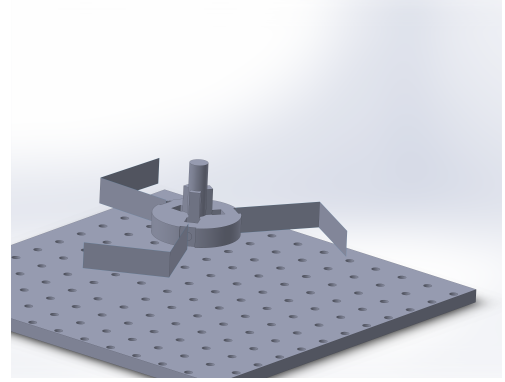
## C Stage design iterations

This section provides some preliminary concepts of a stage guided by helical flexures. In figure 11a different clamping orientations were explored. The second figure (11b) represents a 3DoF planar compliant motion stage for the purpose of comparing with the helical motion stages in figure 12.





(a) Stage set up iteration 1



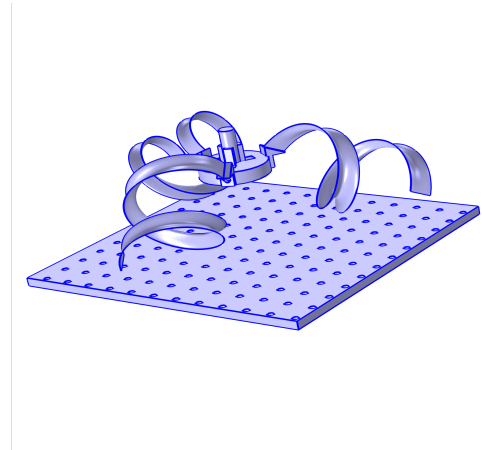
(b) Stage end effector 3 folded leaf

Figure 11: Design process stage surfaces 1

Here are other concepts that also did not converge into a success. Changing the height of the clamping of the helical stage (figure 12a), was intended to have the center of compliance of the individual helical flexure and the end-effector more level to each other. It would be interesting to look further into this. The second figure (12b) had the purpose of also changing the location of the center of compliance. This was done to see if this would change the coupling between the rotations and translations. However, this also did not lead to anything useful.



(a) helix stage higher clamps



(b) helix 1.5 revolution stage

Figure 12: Design process stage surfaces 2

## D Comsol mesh sensitivity

Mesh size influences the accuracy of the simulations. This was important for both eigenfrequency and displacement simulations. The table below shows how the mesh size influences the eigenfrequencies. Triangular mesh elements have been used.

Maximum element size [m]	0.119	0.0711	0.045	0.0237	0.019	0.013
Eigenfrequency	Comsol [Hz]	Comsol [Hz]	Comsol [Hz]	Comsol [Hz]	Comsol [Hz]	Comsol [Hz]
1 <sup>st</sup>	27.3	27.0	27.4	26.6	26.6	26.6
2 <sup>nd</sup>	27.5	27.2	27.6	26.7	26.6	26.6
3 <sup>rd</sup>	41.8	39.4	41.1	40.4	40.3	40.3
4 <sup>th</sup>	51.8	47.7	48.9	49.2	49.1	49.1
5 <sup>th</sup>	52.0	47.8	49.8	49.2	49.1	49.1
6 <sup>th</sup>	72.5	71.9	72.3	70.8	70.6	70.6

Table 1: Eigenfrequencies Comsol model - maximum mesh element size

## E Sensitivity analysis of Comsol models

Comsol Multiphysics software was used for various purposes. One of them was to perform an eigenfrequency analysis of the helical flexure stage. It has been mentioned in the paper that the eigenfrequencies were sensitive towards the thickness parameter. Here are some further calculations giving insight into these sensitivities.

$$\omega_0^2 \propto \frac{stiffness}{inertia} \quad (1)$$

Thickness [mm]	1	1.5	2	2.5	3	3.5
Eigenfrequency	Comsol [Hz]	Comsol [Hz]	Comsol [Hz]	Comsol [Hz]	Comsol [Hz]	Comsol [Hz]
1 <sup>st</sup>	12	19	26.5	32	37.5	42.8
2 <sup>nd</sup>	12	19	26.5	32	37.5	42.8
3 <sup>rd</sup>	23.5	32.7	40	46	51	56
4 <sup>th</sup>	30.3	40.5	49	56	62.7	68.5
5 <sup>th</sup>	30.3	40.5	49	56	62.7	68.5
6 <sup>th</sup>	37	53.5	70.5	82.7	94.5	103

Table 2: Eigenfrequencies Comsol model changing thickness of helical flexures

Increasing the thickness of the helical flexures results in higher eigenfrequencies. This is expected and explained by the fact that stiffness scales cubically with thickness, see equation 1. The eigenfrequencies are very sensitive to this parameter. Similar calculations were done with different length. One would expect the frequencies to increase but not as aggressively as with the thickness.

Furthermore, the percentage of material infill of the end-effect also influences the eigenfrequency of the helical motion stage. It was difficult to accurately model the amount of infill and hence there was some uncertainty about the weight of the end-effector. Furthermore, the end-effector also

carried 3 nuts and 3 thorax M6 bolts. Also adding additional weight. Obviously these nuts and bolts are solids and the model does not take that additional weight into account. In order to see how additional weight affects the eigenfrequency two things were varied. The thickness of the bolts and nuts were increased thereby raising the weight of the nuts and bolts.

Thickness steel [mm]	0.0005	0.001	0.0015	0.002	0.003	0.004
Eigenfrequency	Comsol [Hz]	Comsol [Hz]	Comsol [Hz]	Comsol [Hz]	Comsol [Hz]	Comsol [Hz]
1 <sup>st</sup>	27.6	26.6	25.7	24.8	23.4	22.1
2 <sup>nd</sup>	27.6	26.6	25.7	24.8	23.4	22.1
3 <sup>rd</sup>	40.5	40.3	40.1	39.8	39.4	38.9
4 <sup>th</sup>	49.3	49.1	48.9	48.8	48.6	48.4
5 <sup>th</sup>	49.3	49.1	48.9	48.8	48.6	48.4
6 <sup>th</sup>	71.9	70.6	69.0	67.1	63.3	59.6

Table 3: Eigenfrequencies Comsol model varying weight of thorax bolts and nuts

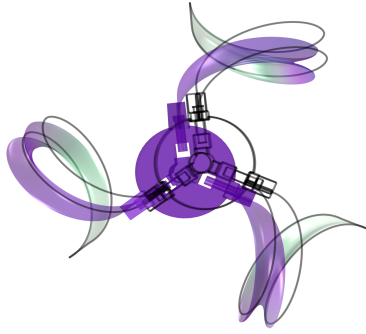
Table 4 indicates that the numerical frequencies become less and converge towards the experimental obtained frequencies. This is expected since additional weight affects the inertia and overall should decrease each eigenfrequency (see equation1).

## F Eigenmodes of Comsol model

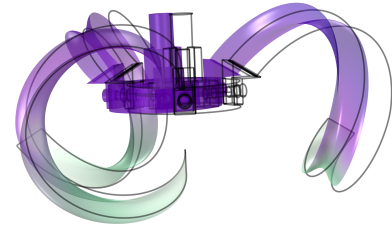
This section gives an visual overview of the eigenmodes for the first six eigenfrequencies. This allows one to see how the kinematic behaviour of the flexure system.



Figure 13: First eigenmode

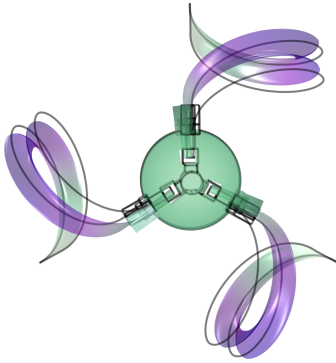


(a) Top view

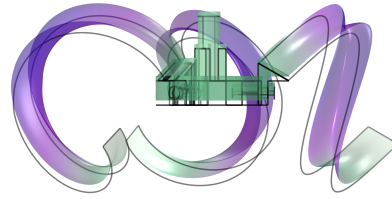


(b) Side view

Figure 14: Second eigenmode

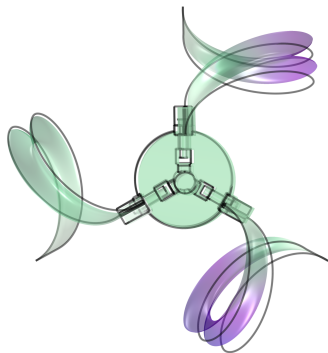


(a) Top view

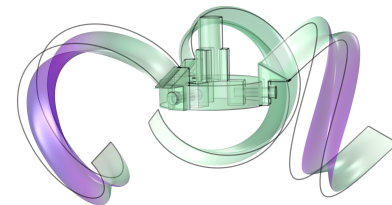


(b) Side view

Figure 15: Third eigenmode

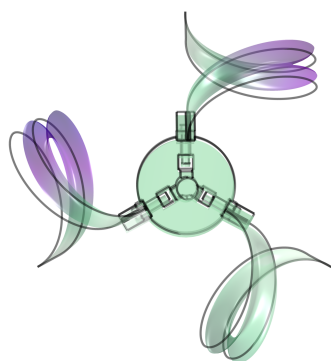


(a) Top view

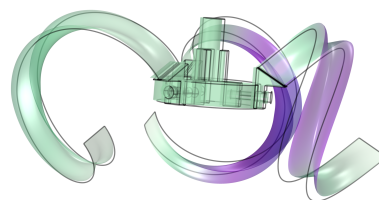


(b) Side view

Figure 16: Fourth eigenmode

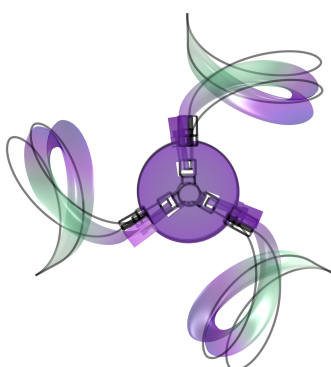


(a) Top view

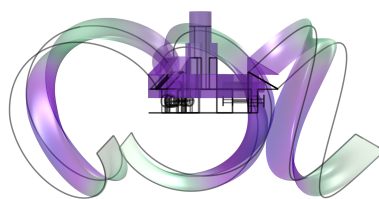


(b) Side view

Figure 17: Fifth eigenmode



(a) Top view



(b) Side view

Figure 18: Sixth eigenmode

## G Comsol pitch calculations

The proposed helical compliant motion stage had 3 DoF. One screw and two orthogonal translations. It was interesting to calculate the approximate value of the pitch value of that screw. Using Comsol multi-physics, forces and moments of various magnitudes were imposed on the end-effector. The displacements and rotations were calculated. One needed to apply small force and moments to make sure that the response was well within the linear regime.

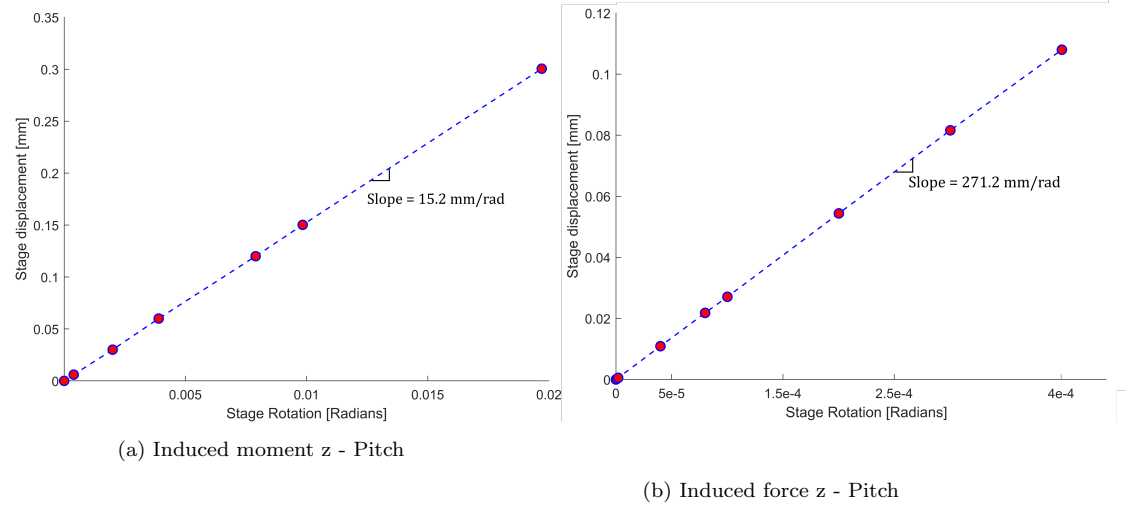


Figure 19: Pitch calculations

Figure 19a shows a plot of stage displacement vs rotation when applying a moment ranging from 0 to 0.25 Nm. The slope is equal to the pitch of the desired screw and is equal to 15.2 mm/rad. For demonstration purposes, applying a 1 degree (0.0175 rad) rotation will result the following displacement:

$$Displacement = pitch \times rotation\ angle = 15.2 \times 0.0175 = 0.265\ mm \quad (2)$$

In other words, a one degree rotation will cause a 0.265 translation in the z-direction.

Figure 19b shows a plot of stage displacement vs rotation when applying a force ranging from 0 to 0.25 N. The slope is equal to the pitch and is equal to 271.2 mm/rad. For demonstration purposes, applying a 1 degree (0.0175 rad) rotation will result the following displacement:

$$Displacement = pitch \times rotation\ angle = 271.2 \times 0.0175 = 4.7\ mm \quad (3)$$

In other words, a one degree rotation will cause a 4.7 mm translation in the z-direction.

The difference in pitch values is a finding that was not expected. Given that the compliance and stiffness matrix is symmetric, one would assume that these values are equivalent. This finding itself still remains uncertain and needs to be investigated further.

## H Symmetry of helical flexure stage

The first two numerical eigenfrequencies show that these two values are very close to each other. This can be explained due to the 'perfect' symmetrical design within this theoretical model. In theory, if one helical flexure has a different thickness or length essentially making the design less symmetrical. The eigenfrequencies should shift further away from each. The following table results of changing one helical flexure while keeping the thickness of the other two constant at 2 mm.

Thickness [mm]	0.001	0.0015	0.002	0.0025	0.003	0.0035
Eigenfrequency	Comsol [Hz]	Comsol [Hz]	Comsol [Hz]	Comsol [Hz]	Comsol [Hz]	Comsol [Hz]
1 <sup>st</sup>	18.1	22.5	26.6	27.6	28.9	30.6
2 <sup>nd</sup>	25.5	25.9	26.6	29.6	31.6	33.2
3 <sup>rd</sup>	30.4	37.5	40.3	42.4	44.5	46.2
4 <sup>th</sup>	40.3	43.5	49.1	49.2	49.4	49.6
5 <sup>th</sup>	47.4	48.8	49.1	53.4	56.6	59.3
6 <sup>th</sup>	55.3	65.6	70.5	75.9	80.3	82.8

Table 4: Eigenfrequencies Comsol model varying weight of thorax bolts and nuts

Table 4 shows the trend that is expected. Most importantly, regardless of making a single helical flexure more or less thick than the other two. A more asymmetrical design pushes the eigenfrequencies to move further apart. A smaller thickness means less stiffness and hence a lower eigenfrequency. Vice versa, a thicker flexure will have a larger stiffness and also an higher eigenfrequency.

## I Second moment of area

This section provides notes and calculations of understanding the analytical stiffness of a cantilever leaf spring. Furthermore, the derivation of second moment of area of an ellipse is shown. This was used to analytically derive the area moment of inertia of an half-hollow-ellipse.

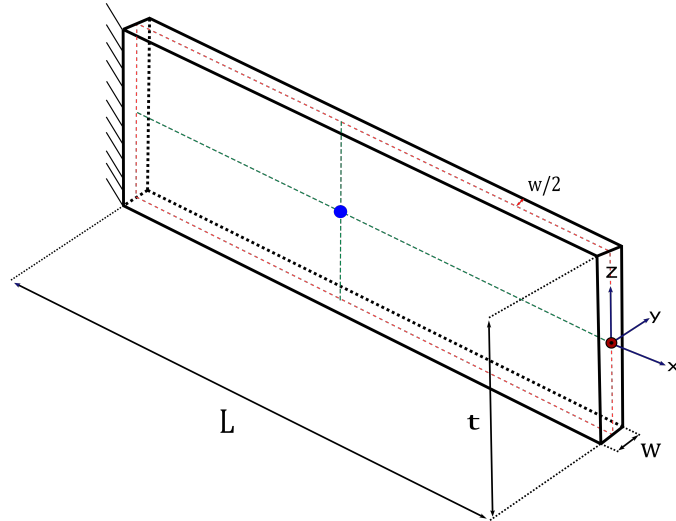


Figure 20: Cantilever leaf spring

Principle Stiffness table

Loading type	In/out of plane	Stiffness	Units
Translation x – axial direction	In-plane	$\frac{EA}{L} = \frac{Ewt}{L}$	$\frac{N}{m}$
Translation y – perpendicular direction	Out-of-plane	$\frac{Et^3}{4L^3} = \frac{3EI_z}{L^3}$	$\frac{N}{m}$
Translation z – transverse direction	In-plane	$\frac{Et^3w}{4L^3} = \frac{3EI_y}{L^3}$	$\frac{N}{m}$
Rotation x – torsion	Out-of-plane	$\frac{Gtw^3}{3L} = \frac{Et^3}{6L(v+1)} = \frac{2EI_z}{L(v+1)}$	$\frac{Nm}{rad}$
Rotation y – bending	Out-of-plane	$\frac{Et^3w}{12L} = \frac{EI_y}{L}$	$\frac{Nm}{rad}$
Rotation z – shear	In-plane	$\frac{Et^3}{12L} = \frac{EI_z}{L}$	$\frac{Nm}{rad}$

$$I_z = \frac{tw^3}{12}, I_y = \frac{t^3w}{12}, G = \frac{E}{2(1+v)}$$

Figure 21: Principle stiffness table leaf

Here is an overview of the calculations required to calculate the second moment of area of an ellipse.

Second moment of area x-axis

$$1 = \frac{x^2}{a^2} + \frac{y^2}{b^2} \quad (4)$$

$$x = \frac{a}{b} \left( \sqrt{b^2 - y^2} \right)$$

$$I_x = \int_{-b}^b \int_0^x y^2 dx dy = \int_{-b}^b [y^2 x]_0^x dy \quad (5)$$

$$I_x = \int_{-b}^b y^2 (x - 0) dy = \int_{-b}^b y^2 x dy$$

$$I_x = \int_{-b}^b y^2 \frac{a}{b} \left( \sqrt{b^2 - y^2} \right) dy \quad (6)$$

$$y = b \sin(\theta)$$

$$dy = b \cos(\theta) d\theta \quad (7)$$

$$y = [-b, b] \quad \theta = \left[ \frac{-\pi}{2}, \frac{\pi}{2} \right]$$

$$I_x = \int_{-\frac{\pi}{2}}^{\frac{\pi}{2}} (b \sin(\theta))^2 \frac{a}{b} \left( \sqrt{b^2 - (b \sin(\theta))^2} \right) b \cos(\theta) d\theta \quad (8)$$

$$\sqrt{b^2 - (b^2 \sin^2(\theta))} = \sqrt{b^2 (1 - \sin^2(\theta))} = \sqrt{b^2 \cos^2(\theta)} = b \cos(\theta)$$



$$I_x = \int_{-\frac{\pi}{2}}^{\frac{\pi}{2}} b^3 a \sin^2(\theta) \cos^2(\theta) d\theta$$

$$\sin^2(\theta) \cos^2(\theta) = \frac{\sin^2(\theta)}{4} \quad (9)$$

$$I_x = \int_{-\frac{\pi}{2}}^{\frac{\pi}{2}} \frac{b^3 a}{4} \sin^2(\theta) d\theta$$

$$I_x = \int_{-\frac{\pi}{2}}^{\frac{\pi}{2}} \frac{b^3 a}{4} \frac{1 - \cos(4\theta)}{2} d\theta \quad (10)$$

$$I_x = \int_{-\frac{\pi}{2}}^{\frac{\pi}{2}} \frac{b^3 a}{4} \frac{1 - \cos(4\theta)}{2 \times 4} d\theta$$

$$I_x = \frac{b^3 a}{32} [(4\theta - \sin(4\theta))_{-\frac{\pi}{2}}^{\frac{\pi}{2}}] \quad (11)$$

$$I_x = \frac{b^3 a}{32} \left[ \left( \frac{4\pi}{2} - \sin\left(\frac{4\pi}{2}\right) \right) - \left( -\frac{4\pi}{2} - \sin\left(-\frac{4\pi}{2}\right) \right) \right] \quad (12)$$

$$I_x = \frac{b^3 a}{32} \frac{8\pi}{2} = \frac{\pi}{8} b^3 a$$

Second moment of area y-axis

$$1 = \frac{x^2}{a^2} + \frac{y^2}{b^2} \quad (13)$$

$$y = \frac{b}{a} \left( \sqrt{a^2 - x^2} \right)$$

$$I_y = \int_0^a \int_{-y}^y x^2 dy dx = \int_a^0 [x^2 y]_0^x dx \quad (14)$$

$$I_y = \int_0^a x^2 (y - (-y)) dx = \int_0^a 2x^2 y dx$$

$$I_y = \int_0^a 2x^2 \frac{b}{a} \left( \sqrt{a^2 - x^2} \right) dx \quad (15)$$

$$x = a \cos(\theta)$$

$$dx = -a \sin(\theta) d\theta \quad (16)$$

$$x = [0, a] \quad \theta = \left[ 0, \frac{\pi}{2} \right]$$

$$I_y = \int_0^{\frac{\pi}{2}} 2 (a \cos(\theta))^2 \frac{b}{a} \left( \sqrt{a^2 - (a \cos(\theta))^2} \right) \times -a \sin(\theta) d\theta \quad (17)$$

$$\sqrt{a^2 - (a^2 \cos^2(\theta))} = \sqrt{a^2 (1 - \cos^2(\theta))} = \sqrt{a^2 \sin^2(\theta)} = a \sin(\theta)$$

$$I_y = \int_0^{\frac{\pi}{2}} -2a^3 b \sin^2(\theta) \cos^2(\theta) d\theta$$

$$\sin^2(\theta) \cos^2(\theta) = \frac{\sin^2(\theta)}{4} \quad (18)$$

$$I_y = \int_0^{\frac{\pi}{2}} -\frac{2a^3 b}{4} \sin^2(\theta) d\theta$$

$$I_y = \int_0^{\frac{\pi}{2}} \frac{2a^3 b}{4} \left( \frac{-1 + \cos(4\theta)}{-2} \right) d\theta \quad (19)$$

$$I_y = \int_0^{\frac{\pi}{2}} \frac{2a^3 b}{4} \left( \frac{-1 + \cos(4\theta)}{-2 \times 4} \right) d\theta$$

$$I_y = -\frac{2a^3 b}{32} [(-4\theta + \sin(4\theta))]_0^{\frac{\pi}{2}} \quad (20)$$

$$I_y = -\frac{2a^3 b}{32} \left[ \left( -\frac{4\pi}{2} + \sin\left(\frac{4\pi}{2}\right) \right) - (0 - 0) \right] \quad (21)$$

$$I_y = \frac{a^3 b}{16} \frac{4\pi}{2} = \frac{\pi}{8} a^3 b$$

## J Quantitative example - SCH flexure

This section will consist of a numerical example of the frequently used SCH (helix 6) flexure mechanism.

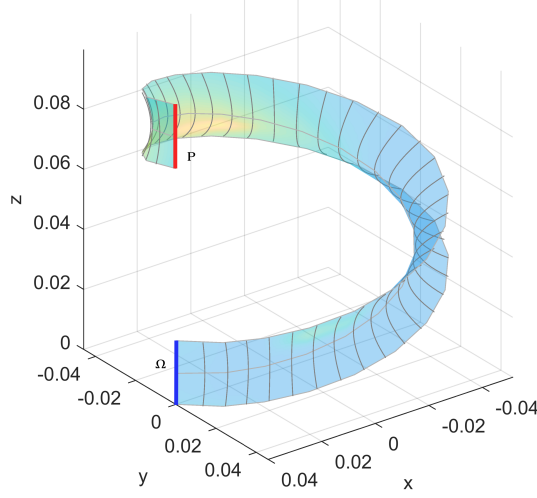


Figure 22: SCH flexure

This has the following tangent compliance matrix,

$$C_t = \begin{bmatrix} 0.0024 & 0.0005 & -0.0013 & -0.0124 & 0.0405 & -0.0020 \\ 0.0005 & 0.0029 & 0.0023 & -0.0451 & -0.0021 & 0.0138 \\ -0.0013 & 0.0023 & 0.0055 & -0.0148 & -0.0458 & 0.0144 \\ -0.0124 & -0.0451 & -0.0148 & 1.2401 & -0.0241 & -0.0376 \\ 0.0405 & -0.0021 & -0.0458 & -0.0241 & 1.0850 & -0.2468 \\ -0.0020 & 0.0138 & 0.0144 & -0.0376 & -0.2468 & 0.8310 \end{bmatrix} \quad (22)$$

$$\mathbf{C} = \begin{bmatrix} \hat{T}_f & \hat{T}_\gamma \end{bmatrix} \begin{bmatrix} a_f & 0 \\ 0 & a_\gamma \end{bmatrix} \begin{bmatrix} \hat{T}_f \\ \hat{T}_\gamma \end{bmatrix} \quad (23)$$

The twist matrix,

$$\begin{bmatrix} \hat{T}_f & \hat{T}_\gamma \end{bmatrix} = \begin{bmatrix} 0.1410 & 0.9875 & 0.0706 & -0.0271 & 0.0146 & -0.0273 \\ 0.8759 & -0.1577 & 0.4560 & -0.0105 & 0.0357 & 0.0117 \\ -0.4615 & 0.0025 & 0.8872 & 0.0187 & 0.0066 & 0.0388 \\ 0 & 0 & 0 & -0.0790 & -0.9896 & -0.1205 \\ 0 & 0 & 0 & -0.5193 & 0.1440 & -0.8424 \\ 0 & 0 & 0 & -0.8510 & 0.0039 & 0.5252 \end{bmatrix} \quad (24)$$

Compliance stationary multipliers,

$$\begin{bmatrix} a_f & 0 \\ 0 & a_\gamma \end{bmatrix} = \begin{bmatrix} 0.0002 & 0 & 0 & 0 & 0 & 0 \\ 0 & 0.0007 & 0 & 0 & 0 & 0 \\ 0 & 0 & 0.0042 & 0 & 0 & 0 \\ 0 & 0 & 0 & 0.6769 & 0 & 0 \\ 0 & 0 & 0 & 0 & 1.2438 & 0 \\ 0 & 0 & 0 & 0 & 0 & 1.2354 \end{bmatrix} \quad (25)$$

This has the following tangent stiffness matrix,

$$K_t = 1 \times 10^3 \begin{bmatrix} 1.4935 & 0.3154 & -0.2622 & 0.0215 & -0.0696 & -0.0168 \\ 0.3154 & 3.3913 & -1.6470 & 0.1037 & -0.0830 & -0.0469 \\ -0.2622 & -1.6470 & 1.1034 & -0.0475 & 0.0572 & 0.0224 \\ 0.0215 & 0.1037 & -0.0475 & 0.0041 & -0.0029 & -0.0015 \\ -0.0696 & -0.0830 & 0.0572 & -0.0029 & 0.0061 & 0.0019 \\ -0.0168 & -0.0469 & 0.0224 & -0.0015 & 0.0019 & 0.0021 \end{bmatrix} \quad (26)$$

$$\mathbf{K} = \begin{bmatrix} \hat{w}_f & \hat{w}_\gamma \end{bmatrix} \begin{bmatrix} k_f & 0 \\ 0 & k_\gamma \end{bmatrix} \begin{bmatrix} \hat{w}_f \\ \hat{w}_\gamma \end{bmatrix} \quad (27)$$

The wrench matrix,

$$\begin{bmatrix} \hat{w}_f & \hat{w}_\gamma \end{bmatrix} = \begin{bmatrix} 0.1410 & 0.9875 & 0.0706 & 0 & 0 & 0 \\ 0.8759 & -0.1577 & 0.4560 & 0 & 0 & 0 \\ -0.4615 & 0.0025 & 0.8872 & 0 & 0 & 0 \\ 0.0269 & 0.0033 & 0.0282 & -0.0790 & -0.9896 & -0.1205 \\ -0.0253 & -0.0385 & 0.0337 & -0.5193 & 0.1440 & -0.8424 \\ -0.0125 & -0.0063 & -0.0115 & -0.8510 & 0.0039 & 0.5252 \end{bmatrix} \quad (28)$$

Stiffness stationary multipliers,

$$\begin{bmatrix} k_f & 0 \\ 0 & k_\gamma \end{bmatrix} = 1 \times 10^3 \begin{bmatrix} 4.3098 & 0 & 0 & 0 & 0 & 0 \\ 0 & 1.4424 & 0 & 0 & 0 & 0 \\ 0 & 0 & 0.2359 & 0 & 0 & 0 \\ 0 & 0 & 0 & 0.0015 & 0 & 0 \\ 0 & 0 & 0 & 0 & 0.0008 & 0 \\ 0 & 0 & 0 & 0 & 0 & 0.0008 \end{bmatrix} \quad (29)$$

Now the RasT unification approach will be implemented, transforming the rotation as an equivalent translation. Hence, all the stationary multipliers will have units of N/m. This example will only show the transformation of the compliance matrix as the stiffness is simply its inverse.

$$\tilde{a}_{fi} = \chi_i^2 a_{\gamma i} \quad (30)$$

$$\tilde{a}_{fi} = (|r_i|^2 + h_i^2) a_{\gamma i} \quad (31)$$

Pitch values,

$$\begin{bmatrix} h_1 \\ h_2 \\ h_3 \end{bmatrix} = \begin{bmatrix} -0.0083 \\ -0.0093 \\ 0.0138 \end{bmatrix} \quad (32)$$

Location vectors twist that are normalized,

$$\begin{bmatrix} |r_1| \\ |r_2| \\ |r_3| \end{bmatrix} = \begin{bmatrix} 0.0336 \\ 0.0380 \\ 0.0468 \end{bmatrix} \quad (33)$$

Unification variable  $\chi_i^2$ ,

$$\begin{bmatrix} \chi_1^2 \\ \chi_2^2 \\ \chi_3^2 \end{bmatrix} = \begin{bmatrix} (|r_1|^2 + h_1^2) \\ (|r_2|^2 + h_2^2) \\ (|r_3|^2 + h_3^2) \end{bmatrix} = \begin{bmatrix} 0.0012 \\ 0.0015 \\ 0.0024 \end{bmatrix} \quad (34)$$

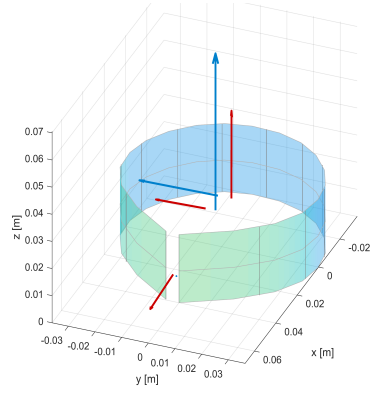
$$\tilde{\mathbf{a}}_f = \begin{bmatrix} a_{fi} & 0 \\ 0 & (|r_i|^2 + h_i^2) a_{\gamma i} \end{bmatrix} \quad (35)$$

$\tilde{\mathbf{a}}_f$  represents the unified stationary compliance multipliers. Note, that its inverse is equivalent to the stiffness unified stationary multipliers.

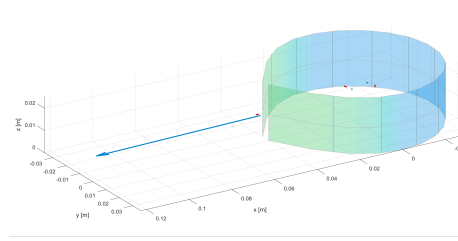
$$\tilde{\mathbf{a}}_f = \begin{bmatrix} 0.0002 & 0 & 0 & 0 & 0 & 0 \\ 0 & 0.0007 & 0 & 0 & 0 & 0 \\ 0 & 0 & 0.0042 & 0 & 0 & 0 \\ 0 & 0 & 0 & 0.0008 & 0 & 0 \\ 0 & 0 & 0 & 0 & 0.0019 & 0 \\ 0 & 0 & 0 & 0 & 0 & 0.0029 \end{bmatrix} \quad (36)$$

$$\mathbf{C} = \begin{bmatrix} \hat{T}_f & \hat{T}_\gamma \end{bmatrix} \begin{bmatrix} I & 0 \\ 0 & \frac{1}{\sqrt{|r_i|^2 + h_i^2}} \end{bmatrix} \tilde{\mathbf{a}}_f \begin{bmatrix} I & 0 \\ 0 & \frac{1}{\sqrt{|r_i|^2 + h_i^2}} \end{bmatrix} \begin{bmatrix} \hat{T}_f \\ \hat{T}_\gamma \end{bmatrix} \quad (37)$$

## K Unified stiffness and compliance visualization

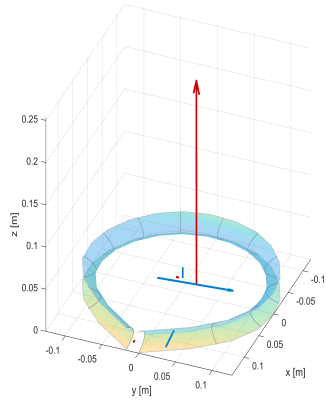


(a) Unified Compliance - Helix 1

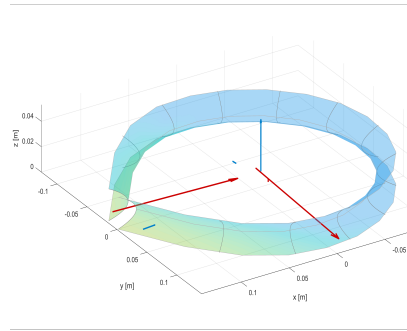


(b) Unified stiffness - Helix 1

Figure 23: Unified eigen-system

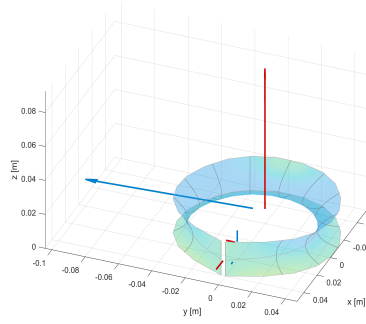


(a) Unified Compliance - Helix 2

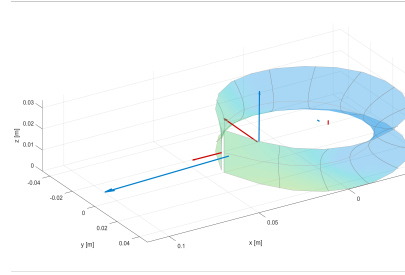


(b) Unified stiffness - Helix 2

Figure 24: Unified eigen-system

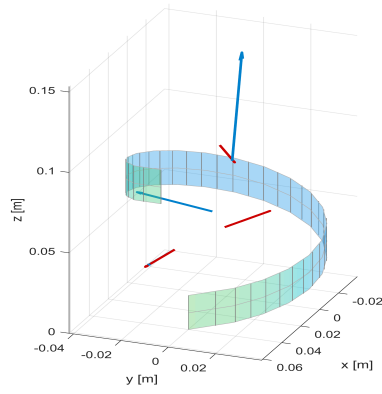


(a) Unified Compliance - Helix 3

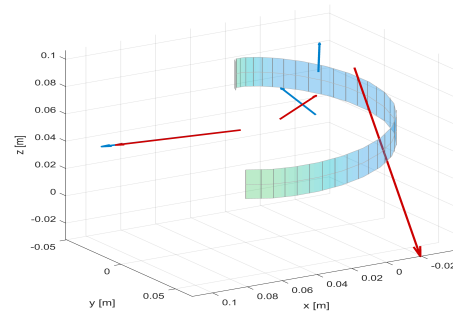


(b) Unified stiffness - Helix 3

Figure 25: Unified eigen-system

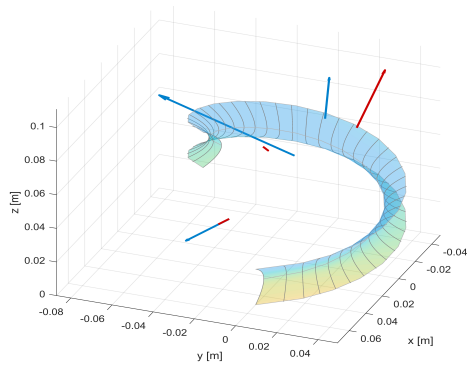


(a) Unified Compliance - Helix 4

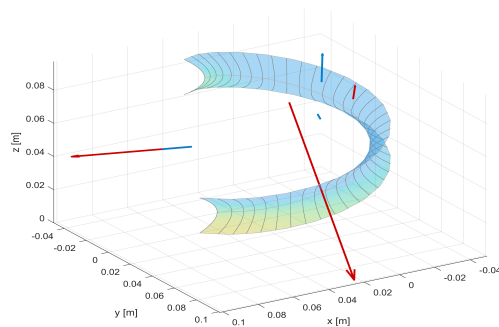


(b) Unified stiffness - Helix 4

Figure 26: Unified eigen-system



(a) Unified Compliance - Helix 5



(b) Unified stiffness - Helix 5

Figure 27: Unified eigen-system

